Mid-lithospheric discontinuities and complex anisotropic layering in the mantle lithosphere beneath the Wyoming and Superior Provinces

Heather A. Ford[1,2,*], Maureen D. Long[1] and Erin A. Wirth[3]

[1]Department of Geology and Geophysics, Yale University, New Haven, CT, USA.
[2]Now at: University of California – Riverside, Riverside, CA, USA.
[3]University of Washington, Seattle, WA, USA.

To be submitted to Journal of Geophysical Research – Solid Earth

*Corresponding author:
Department of Earth Sciences , University of California - Riverside
900 University Avenue, Riverside, California, 92521
E-mail: heather.ford@ucr.edu.

Key Points:

1. Location of anisotropic boundaries inferred from Ps receiver function analysis
2. Numerous anisotropic boundaries with varying geometries are observed but do not necessarily overlap with inferred MLD
3. Results vary regionally (within and across cratons), suggesting complex deformation histories

Abstract

The observation of widespread seismic discontinuities within Archean and Proterozoic lithosphere is intriguing, as their presence may shed light on the formation and early evolution of cratons. A clear explanation for the discontinuities, which generally manifest as a sharp decrease in seismic velocity with depth, remains elusive. Recent work has suggested that mid-lithospheric discontinuities (MLDs) may correspond to a sharp gradient in seismic anisotropy, produced via deformation associated with craton formation. Here we test this hypothesis beneath the Archean Superior and Wyoming Provinces using anisotropic Ps receiver function (RF) analysis to characterize the relationship between MLDs and seismic anisotropy. We computed radial and transverse component RFs for 13 long-running seismic stations. Of these, six stations with particularly clear signals were analyzed using a harmonic regression technique. In agreement with previous studies, we find evidence for multiple MLDs within the cratonic lithosphere of the Wyoming and Superior Provinces. Our harmonic regression results reveal that 1) MLDs can be primarily explained by an isotropic negative velocity gradient, 2) multiple anisotropic boundaries exist within the lithospheric mantle, 3) the isotropic MLD and the anisotropic boundaries do not necessarily occur at the same depths, and 4) the depth and geometry of the anisotropic boundaries vary among stations. We infer that the MLD does not directly correspond to a change in anisotropy within the mantle lithosphere. Furthermore, our results reveal a surprising level of complexity within the cratonic lithospheric mantle, suggesting that the processes responsible for shaping surface geology produce similar structural complexity at depth.

1. Introduction

A defining characteristic of the cratonic upper mantle is the faster than average seismic wave speeds down to depths of 150-200 km or more, as evidenced by tomographic models [e.g., *Kustowski et al.,* 2008; *Nettles and Dziewonski,* 2008; *Simmons et al.,* 2010; *Lekic and Romanowicz,* 2011; *Ritsema et al.,* 2011; *French et al.,* 2013; *Moulik and Ekström*, 2014; *Schaeffer and Lebedev,* 2014]. The fast velocities are likely due to a number of factors, including cooler temperatures and a larger degree of chemical depletion [e.g., *Jordan,* 1978; *Griffin et al.,* 1999; *James et al.,* 2004; *Lee,* 2006]. As a result, the cratons have a neutrally buoyant mantle keel [*Jordan,* 1978], capable of withstanding thermal, mechanical and chemical erosion over long time periods [e.g., *Lenardic and Moresi,* 1999; *Shapiro et al.,* 1999; *King,* 2005].

Within the cratonic mantle there is evidence for widespread, discrete, negative velocity gradients (that is, a velocity decrease with increasing depth) at depths of 80 to 150 km [*Dueker et al.*, 2001; *Thybo*, 2006; *Wittlinger and Farra,* 2007; *Chen,* 2009; *Rychert and Shearer,* 2009; *Abt, et al.,* 2010; *Fischer et al.,* 2010; *Ford et al.,* 2010; *Miller and Eaton,* 2010; *Kind et al.,* 2012; *Kumar et al.,* 2012, 2013; *Wolbern et al.,* 2012; *Bodin et al.,* 2013; *Hansen et al.,* 2013; *Lekic and Fischer,* 2014; *Sodoudi et al.,* 2013; *Foster et al.,* 2014; *Hopper et al.,* 2014; *Hopper and Fischer,* 2015; *Porritt et al.,* 2015]. These negative velocity gradients are commonly referred to as mid-lithospheric discontinuities (MLDs). The term was originally defined by *Abt et al.* [2010] using Sp receiver function analysis in North America; however, a mid-lithospheric negative velocity gradient has also been referred to as the 8° discontinuity [e.g., *Chu et al.*, 2012]. Mid-lithospheric discontinuities have been the subject of intense interest in part because of their appearance in old and tectonically stable continental lithosphere, as well as their near ubiquity [see *Selway et al.* [2015] for a review]. Several different mechanisms have been proposed to account for the presence of MLDs in the lithosphere, including a change in composition [e.g., *Ford et al.,* 2010; *Yuan and Romanowicz,* 2010; *Wolburn et al.,* 2012; *Sodoudi et al.,* 2013; *Foster et al.,* 2014; *Hopper and Fischer,* 2015], a transition to anelastic grain boundary sliding [*Karato,* 2012; *Karato et al.,* 2015], and a boundary in seismic anisotropy [*Yuan et al.,* 2011; *Sodoudi et al.,* 2013; *Wirth and Long,* 2014], perhaps due to inherited deformation structures [e.g., *Cooper and Miller,* 2014]..

While the presence of "frozen-in" anisotropic structure in the mantle lithosphere due to past tectonic events has been well established [e.g., *Silver,* 1996; *Savage,* 1999; *Fouch and Rondenay,* 2006], more recent work has focused on the possible connection between the MLD and gradients in azimuthal anisotropy [*Yuan et al.,* 2011; *Wirth and Long,* 2014]. One significant issue in attributing MLDs solely to contrasts in seismic anisotropy with depth is that while MLDs appear to be ubiquitous, variations in azimuthal anisotropy in the mantle lithosphere are thought to arise from regional tectonic processes [e.g., *Bostock,* 1998; *Simons and van der Hilst,* 2003; *Silver et al.,* 2004; *Fouch and Rondenay,* 2006]. It is also unclear as to how a boundary in azimuthal anisotropy (in the absence of an isotropic wavespeed gradient) can produce a consistently negative phase in Sp receiver function analysis, the most frequently used MLD imaging tool [*Selway et al.,* 2015], and more work is required to understand the effects of anisotropy on S-to-P converted phases.

Receiver function (RF) analysis is a seismic imaging method used to characterize discontinuities within the crust, upper mantle and transition zone [e.g., *Langston,* 1979].

The method relies on the partial scattering of an incoming wave to a converted phase to infer information about the depth and impendence contrast of the seismic boundary. In practice this is done through the deconvolution of the incoming wave (e.g., P for Ps) from the scattered phase component (e.g., radial or transverse for Ps), thus removing instrument and source effects. A distinct advantage of this analysis relative to other methods, such as surface wave tomography or shear wave splitting analysis, is the sensitivity of receiver functions to sharp gradients in structure with depth (that is, seismic discontinuities), making it ideal for use in regions where multiple layers or depth-dependent anisotropy are thought to exist.

A number of different phases can be used to compute receiver functions, including direct telesesimic P-waves [e.g., *Bostock,* 1998; *Li et al.,* 2000; *Collins et al.,* 2002; *Rychert et al.,* 2005; *Chen et al.,* 2006; *Rychert and Shearer,* 2009; *Ozacar et al.,* 2008; *Abt et al.,* 2010; *Ford et al.,* 2010; *Wirth and Long,* 2012, 2014] and S-waves [e.g., *Oreshin et al.,* 2002; *Vinnik et al.,* 2005; *Sodoudi et al.,* 2006; *Heit et al.,* 2007; *Kumar et al.,* 2007; *Li et al.,* 2007; *Hansen et al.* 2009; *Abt et al.,* 2010; *Ford et al.,* 2010, 2014; *Lekic and Fischer,* 2014; *Hopper et al.,* 2014]. One advantage of P-to-S (Ps) receiver function analysis is that the behavior of the receiver functions in the presence of anisotropy is well known [e.g., *Levin and Park,* 1997, 1998; *Savage,* 1998; *Bostock,* 1998; *Fredericksen and Bostock,* 2000]. More specifically, at a flat-lying, isotropic boundary, coupling between the P and SV wavefields results in P-to-SV scattering. When anisotropy is present, coupling occurs between P-SV, and SH waves. Ps receiver function analysis can utilize these conversions by calculating both the radial (P-SV) and transverse (P-SH) component receiver functions. This type of analysis has been used to characterize anisotropic structure in a number of tectonic settings [e.g., *Bostock,* 1998; *Park et al.,* 2004; *Schulte-Pelkum et al.,* 2005; *Mercier et al.,* 2008; *Snyder,* 2008; *Nikulin et al.,* 2009; *Ozacar and Zandt,* 2009; *Porter et al.,* 2011; *Song and Kim,* 2012; *Wirth and Long,* 2012, 2014; *Yuan and Levin,* 2014].

In this study we utilize Ps anisotropic receiver function analysis to image isotropic and anisotropic structure within the Wyoming and Superior Provinces of continental North America. The primary objective in this analysis is to characterize the relationship between the inferred MLD and any observed anisotropy, in hopes of better understanding the origin of the MLD and the processes involved in the formation and early evolution of the continental lithosphere. In particular, we aim to test the hypothesis that the MLD corresponds to, or is co-located with, a contrast in seismic anisotropy at depth within continental lithosphere, as suggested by previous studies [*Yuan et al.,* 2011; *Wirth and Long,* 2014].

2. Tectonic setting

Laurentia, the core of the present-day North American continent, was formed during the Paleoproterozoic when several Archean-aged cratons were assembled through a series of accretionary events [e.g., *Hoffman,* 1988; *Whitmeyer and Karlstrom,* 2007]. The most significant of these was the Trans-Hudson orogeny, which lasted from 1.85-1.78 Ga [*Whitmeyer and Karlstrom,* 2007]. The Archean elements included the Hearne, Superior, and Wyoming Provinces, along with several smaller fragments including the Medicine Hat Block [*Whitmeyer and Karlstrom,* 2007]. Today, the Wyoming craton is located primarily within Wyoming and Montana, while the Superior craton is set within the upper Midwest and in parts of present day Ontario, Quebec and eastern Manitoba (Figure 1).

The histories of the Superior and Wyoming cratons extend well into the Archean, with unique but complimentary modes of formation. The Superior province is composed of a number of Neo- to Mesoarchean (2.5-3.4 Ga) subprovinces, ranging from high-grade gneiss in the northern and southern portions of the province to interlacing plutonic, volcano-plutonic and metasedimentary regions in its center [e.g., *Card,* 1990]. The subprovinces are generally east-west trending and are divided by faults that extend across the width of the province, and are frequently correlated with Moho offsets at depth and north-dipping structure [*Hall and Brisbin,* 1982; *Musacchio et al.,* 2004; *Percival et al.,* 2006], supporting a model of progressive accretion.

Similar to the Superior, the Wyoming province is itself composed of three subprovinces, with the oldest, the Montana metasedimentary province, having rock ages of 3.3-3.5 Ga [*Mueller et al.* 1993]. The Southern Accreted Terranes to the south are the youngest in age and are thought to be the result of magmatic activity occurring along an active margin [*Frost et al.,* 1998]. Situated to the north of the Wyoming province, and separated by the Great Falls Tectonic Zone (GFTZ), is the Archean-aged Medicine Hat Block. The relationships among the Wyoming Craton, Medicine Hat Block and GFTZ are somewhat unclear, with some interpreting the Medicine Hat Block as belonging to the Hearne Province to the north prior to collision with the Wyoming Craton [*Boerner et al.,* 1998]. An alternative interpretation is that the Medicine Hat Block is more closely affiliated with the Wyoming Province [*Eaton et al.,* 1999]. The GFTZ is defined as a series of northeast trending geologic features, including faults [*O'Neill and Lopez,* 1985], which have been described as being due to a deep-seated, lithospheric-scale suture or intracontinental shear zone [*Boerner et al.,* 1998].

The tectonic evolution of the Wyoming and Superior provinces has varied considerably since the Proterozoic. While the Superior Province experienced Grenville-aged rifting (~1.1 Ga) [e.g., *Schmus and Hinze,* 1985; *Whitmeyer and Karlstrom,* 2007], the Wyoming Craton was modified by Laramide-aged basement-cored uplifts [e.g., *Dickinson,* 1985]. The deformation resulting from the Laramide Orogeny included the uplift of many present-day mountain ranges in the Wyoming-Montana region, including the Beartooth Mountains in south central Montana, the Wind River Range in west central Wyoming, the Bighorn Mountains in north central Wyoming, and the Black Hills of western South Dakota. As a result of the tectonic activity, Cretaceous-aged marine sediments can now be found at an average elevation of 2 km [*Cross and Pilger*, 1978]. Deformation-related structures of the Laramide are generally well characterized in the shallow to deep crust [*Smithson et al.,* 1979; *Brewer et al.,* 1980; *Allmendinger et al.,* 1982], and to a lesser extent at the Moho and in the uppermost mantle [e.g., *Snelson et al.,* 1998; *Hansen and Dueker,* 2009; *Yeck et al.,* 2014]. Lithospheric modification in deeper parts of the mantle lithosphere have also been proposed [*Bird*, 1984]. Seismic tomography results indicate that both the Wyoming and Superior cratons are underlain by high velocity lithosphere to depths of 150 km or more, although there is some suggestion that wave speeds are generally slower beneath the Wyoming than the Superior [e.g., *Schaeffer and Lebedev,* 2014].

3. Data and methods

3.1 Data

We selected 13 broadband seismic stations from three different seismic networks (US, CN, TA) within the Wyoming and Superior craton regions for analysis (Figure 1). Station selection was based on the length of operation and relative geographical distribution. Ideally, stations would have 10+ years of data. In the case of several stations only ~9 years of data was available (AGMN, ECSD, EGMT, MDND) and in two cases, less than 8 years of data (K22A and SUSD). Waveform data was acquired from the Incorporated Research Institutions for Seismology (IRIS) Data Management Center (DMC) using the Standing Order for Data (SOD) tool [*Owens et al.,* 2004], available at http://www.seis.sc.edu/sod/. We selected events of magnitude Mw>=5.8, to ensure a good signal to noise ratio, from epicentral distances between 30° and 100° (Figure 2). The number of events used at each station, listed in Table 1, depends on the number of years of available data as well as waveform quality.

3.2 Preprocessing

In order to prepare the data for RF analysis, we first cut waveforms to equal length, then rotated into the radial, transverse and vertical orientations and bandpass filtered between 0.02-2 Hz. Seismograms were visually inspected for an unambiguous P-wave arrival on the vertical and clear radial and transverse components using PASSCAL Quick Look (PQL), and the direct-P arrival for each event was manually picked using the Seismic Analysis Code (SAC). Prior to deconvolution, the components were rotated into the LQT reference frame to account for non-vertical incidence of the incoming direct P-wave [e.g., *Rondenay,* 2009]. Without this correction, energy that should be mapped entirely on the radial component (i.e. P-to-S conversions) will be partially mapped onto the vertical component. The rotation requires the assumption of a near-surface P-wave velocity, which was set to 6.5 km/s or 3.5 km/s, depending on whether or not the station is located within a sedimentary basin. Although all receiver function examples and results shown in this paper were calculated using the LQT coordinate system, for simplicity we refer to them hereinafter using the common terminology of radial and transverse component receiver functions.

3.3 Receiver function methodology

Receiver functions were calculated using a frequency domain multitaper correlation technique, referred to here as the multitaper method (MTM) [*Park and Levin,* 2000]. In contrast to frequency domain deconvolution techniques that use spectral division and water level stabilization [e.g., *Bostock,* 1998], the deconvolution in MTM is achieved using a least-squares correlation between the eigenspectra of the R, T, and Z (more precisely, L, Q, and T) components. Before RF computation, waveforms were bandpass filtered with a high pass cutoff of 0.02 Hz and a variable low pass cutoff of 0.5, 0.75 or 1 Hz. After the individual RFs were calculated they were corrected for variations in slowness (i.e., epicentral distance) and stacked. For each station in our analysis, we first computed a single station radial component stack. We subsequently binned radial and transverse component RFs as a function of epicentral distance and back azimuth, using a bin spacing of 10° for both. Within each bin the individual RFs were weighted according to their uncertainties, which were estimated by the coherence between the LQT components in the frequency domain [*Park and Levin*, 2000]. We did not calculate quantitative uncertainties for summed RFs in single-, epicentral distance- and backazimuth-binned stacks; however, uncertainties were quantified during the harmonic decomposition analysis via a bootstrap approach (see section 3.4).

One significant limitation of the MTM is that the amplitude of the time series tapers off with increasing time, becoming unsuitable for delay times greater than 10 seconds (after the direct P arrival) [*Helffrich,* 2006]. While this does not present a problem for studies of crustal or uppermost mantle structure [e.g., *Liu et al.,* 2015], it is problematic for greater target depths. The precise time window suitable for analysis varies depending on the input parameters used; a more complete discussion is contained in *Park and Levin* [2000]. In this study the analysis window (T) was set to 65 seconds, which significantly affects amplitudes at times greater than 9.75 seconds.

One workaround to the time window limitation is to set the target analysis window to larger delay times; however, this approach yields incomplete results at small delay times. To address this limitation, we calculated the binned and summed RFs over a range of target delay times, specified as target depth, from 0 to 150 km, in 15 km increments. The receiver functions for each of the targeted depths were then spliced to form a single, continuous receiver function; the AK135 reference model [*Kennett et al.*, 1995] was used to transform the target depth to an estimated time window used for the splicing.

3.4 Modeling anisotropy with harmonic stacking

Key to the analysis of anisotropic receiver functions is the understanding of how boundaries in anisotropy produce systematic azimuthal variations in amplitude and polarity on the transverse component [e.g., *Levin and Park,* 1998; *Maupin and Park,* 2007; *Eckhardt and Rabbel,* 2011]. For example, at a boundary where isotropy transitions to a layer of horizontally oriented anisotropy, the amplitude variations with backazimuth on the transverse component follow what is commonly referred to as a four-lobed pattern, i.e., the polarity is flipped every 90° (an example is shown in Figure 3b). In the case of a dipping isotropic interface or a dipping anisotropic symmetry axis, a two-lobed pattern is observed, i.e. a polarity change every 180° (Figure 3b).

In practice, visually identifying changes in amplitude as a function of back azimuth in real data can be challenging. Harmonic decomposition analysis [*Shiomi and Park, 2008*; *Bianchi et al.* 2010; *Liu et al.,* 2015] can overcome the practical limitations of identifying changes in amplitude and polarity at a given delay time by performing a linear regression utilizing information from both radial and transverse component RFs. To perform the analysis, the amplitudes at a given delay time are modeled as being the result of the scaled summation of $\cos(k\theta)$ and $\sin(k\theta)$ terms, where k=0,1,2 and refers to the harmonic order, and θ corresponds to backazimuth. The constant term, k=0, signifies no dependence of amplitude on backazimuth and implies isotropic structure; k=1 and k=2 represent a two- and four-lobed pattern of amplitude/polarity, respectively. The relationship between amplitude, backazimuth and harmonic order is given by *Bianchi et al.* [2010] and is expressed below:

$$
\begin{pmatrix} R_1(t) \\ R_2(t) \\ R_1(t) \\ R_n(t) \\ \cdots \\ T_2(t) \\ \cdots \\ T_n(t) \end{pmatrix} = \begin{pmatrix}
1 & \cos(\theta_1) & \sin(\theta_1) & \cos(2\theta_1) & \sin(2\theta_1) \\
1 & \cos(\theta_2) & \sin(\theta_2) & \cos(2\theta_2) & \sin(2\theta_2) \\
\cdots & \cdots & \cdots & \cdots & \cdots \\
1 & \cos(\theta_n) & \sin(\theta_n) & \cos(2\theta_n) & \sin(2\theta_n) \\
0 & \cos(\theta_1 + \pi/2) & \sin(\theta_1 + \pi/2) & \cos(2\theta_1 + \pi/2) & \sin(2\theta_1 + \pi/2) \\
0 & \cos(\theta_2 + \pi/2) & \sin(\theta_2 + \pi/2) & \cos(2\theta_2 + \pi/2) & \sin(2\theta_2 + \pi/2) \\
\cdots & \cdots & \cdots & \cdots & \cdots \\
0 & \cos(\theta_n + \pi/2) & \sin(\theta_n + \pi/2) & \cos(2\theta_n + \pi/2) & \sin(2\theta_n + \pi/2)
\end{pmatrix} \times
$$

$$
\begin{pmatrix} A(t) \\ B(t) \\ C(t) \\ D(t) \\ E(t) \end{pmatrix},
$$

where R and T correspond to the radial and transverse component amplitudes at a given delay time for *n* given receiver functions, and A(t), B(t), C(t), D(t), and E(t) are the coefficients for the sin(*k*θ)and cos(*k*θ) terms. In this study, we applied the harmonic stacking technique to selected stations with particularly good backazimuthal coverage and clear RF signals, in order to discriminate among isotropic velocity changes, changes in the orientation of anisotropy, and dipping interfaces as potential causes of RF arrivals.

To illustrate the relationships among anisotropic structure, receiver functions, and harmonic stacking we have computed receiver functions from synthetic seismograms [*Fredriksen and Bostock*, 2000] for three specific cases (Figure 3), which include changes in bulk velocity, as well as changes in anisotropy (both horizontal and dipping). For the first example (Figure 3; left hand column), a velocity increase is accompanied by a boundary in horizontally aligned anisotropy, with the fast axis of anisotropy oriented at 90°. Since we observe a bulk (positive) change in velocity, a positive phase is observed along the radial component. Changes to the amplitude of the positive phase, in conjunction with the four-lobed pattern exhibited on the transverse component, indicate that horizontally aligned anisotropy is present. This pattern finds expression in the harmonic decomposition, where energy is present on the constant term (k=0) due to the bulk change in velocity, as well as the cos(2θ) term. In the second example (Figure 3; middle column), the horizontal anisotropy is replaced by dipping anisotropy and the four-lobed pattern becomes a two-lobed pattern with energy within the harmonic stack now present primarily on the constant and sin(θ) components, with a small amount of energy observed on the cos(2θ) component. Finally, we demonstrate the case where the interface in question is purely isotropic, but includes a dipping interface (Figure 3; far right column). The two-lobed pattern is again observed, with energy mapped onto the cos(θ) term. Additionally, a two-lobed pattern, with a polarity opposite the phase associated with the interface, is seen at 0 seconds delay time, and is a characteristic of dipping isotropic interfaces. This is characteristic manifests itself in the cos(θ) term as a phase at 0 seconds delay time with a polarity opposite of the phase corresponding to the interface.

4. Results

We calculated Ps receiver functions for thirteen stations within (or near the boundaries of) the Wyoming and Superior Provinces. Of the thirteen stations, ten yielded interpretable results. This assessment was based on clear (although sometimes complex) Moho arrivals, a lack of "ringy" oscillations that are likely associated with the arrival of multiply scattered phases within the sedimentary column [e.g., *Ford et al.,* 2010], and a sufficient back azimuthal distribution of data. The three stations at which no further analysis was performed were LKWY, located in the Yellowstone Caldera, and MDND and SUSD, which are both located within the Williston Basin. While we do not interpret them further, the radial and transverse component RFs for these stations are included in the supplementary materials.

Here we describe the RF results at the remaining ten stations, with an initial emphasis on the isotropic structure and a subsequent focus on the anisotropic structure, as inferred from the harmonic stacking analysis. In particular, we focus on the detailed interpretation of structure beneath six stations with excellent backazimuthal coverage and particularly clear RF traces; at these stations, we discuss the RF results and the modeling using harmonic decomposition in some detail. In order to illustrate the range of stacking approaches and plotting conventions that we discuss in this section, we show in Figure 4 an example of RF results for a selected station (RSSD), including a single-bin radial RF stack, radial and transverse RFs plotted as a function of back azimuth, the modeled and unmodeled structure derived from the harmonic stacking analysis, and so-called rose plots [e.g., *Wirth and Long,* 2014] that illustrate the variations in transverse component amplitude as a function of backazimuth for selected times.

4.1. Overview of isotropic structure

Single-binned, radial component RFs computed with a low pass filter cutoff of 0.75 Hz for ten stations are shown in Figure 5. From these stacked RFs, we picked the positive arrival that most likely corresponds to the Moho; these are marked on Figure 5 and listed (as delay time in seconds) in Table 1. We also calculated and listed approximate Moho depths (in km) estimated from the 1D AK135 velocity model [*Kennett et al.,* 1995]. We emphasize, however, that these depth estimates are approximate, and do not take into account 3D velocity structure and other potential complexities which can change interface depth estimates by 5 km or more [e.g., *Lekic et al.,* 2011]. However, the focus of this study is on mid-lithospheric discontinuities, and uncertainties estimates of LAB depth from tomography models are likely larger than any associated error from choosing AK135 as our migration model. At some stations, reverberations from thick sedimentary sequences likely interfere with the Moho phase arrival [e.g., *Yeck et al.* 2013]. The average Moho arrival delay time among the ten stations analyzed is 5.4 s (~50 km), with a range of 3.9 s (ULM) to 6.5 s (LAO).

We also picked delay times (and approximate depths) for negative phases that arrive after the Moho phase (and may correspond to MLDs or the LAB) from the stacked radial RFs, as shown in Figure 5 and listed in Table 1. While previously estimated depths to the lithosphere-asthenosphere boundary (LAB) in our study region vary, surface wave tomography results show that high velocity lithosphere extends to depths of ~200 km beneath our study area [e.g., *Porritt et al.,* 2015]. Estimates based on Sp receiver functions put the LAB at depths of 150-200 in the western half of our study area and 200-240 km in the eastern half [*Foster et al.,* 2014], or else do not observe a coherent LAB phase [*Abt et al.,* 2010; *Hopper and Fischer,* 2015]. At stations in our study, all of the negative phases imaged beneath the Moho correspond to an estimated depth of ~160 km or less, so we infer that these generally correspond to discontinuities within the mantle lithosphere itself. (There may be exceptions at stations such as K22A and EGMT in the westernmost part of our study area, where lithospheric thicknesses are smaller and the deeper discontinuities we infer may correspond to the LAB; even at these stations, however, we see also see evidence for shallower discontinuities within the lithosphere, Figure 4). To ensure that we are not incorrectly interpreting crustal or sedimentary basin multiples (reverberations) as lithospheric structure, we also calculated the predicted arrival time of the multiples using the approximated depth of the Moho phase (and in one case the sediment-basement boundary phase) from the Ps receiver function. We see evidence for multiple MLDs at most stations; phases due to conversions at these discontinuities arrive over a range of times, with average values around ~9.4 s (91 km) and ~13.7 s (134 km) delay time, for the shallower and deeper MLD phases, respectively. Our inference of multiple MLDs beneath the Wyoming and Superior cratons is consistent with the recent work of *Hopper and Fischer* [2015].

4.2. Overview of anisotropic structure inferred from harmonic stacking

Sharp gradients in seismic anisotropy with depth have systematic effects on phase amplitude and timing on radial component RFs, but their effects are more readily apparent (and distinguishable from the effects of isotropic discontinuities) on the transverse components (see example in Figure 4). As discussed above, harmonic decomposition of both radial and transverse component RFs is a particularly useful tool for modeling the competing effects of flat-lying isotropic boundaries, dipping interfaces or dipping anisotropy, and flat-lying contrasts in anisotropic structure. In this study, we utilize harmonic stacking to aid us in the identification of potential boundaries in anisotropy.

Figures 5 and 6 illustrate the results of harmonic decomposition for a subset of six highest-quality stations: three from the Wyoming Province and three from the Superior Province. This selection of stations allows us to assess the variability both within and between each province. For each station, we show the amplitudes of the different harmonic expansion terms as a function of delay time, along with the portion of the signal that cannot be modeled by a combination of cos($k\theta$) and sin($k\theta$) terms. Uncertainties for each of the terms were estimated using a bootstrap resampling method (resampled 100 times). Delay times shown in Figures 5 and 6 are relative to that expected for an arrival originating at 90 km depth, rather than relative to the direct P arrival (the convention used in Figures 3-4 and 7-12). To minimize confusion, in the text we refer to the delay times relative to the direct P arrival.

The absolute value of the amplitudes for each of the four non-constant terms (that is, the cos($k\theta$) and sin($k\theta$) terms, where k=1,2) were summed at each delay time in order to determine where coherent peaks in energy occur. These amplitude maxima are marked with gray lines in Figures 5-12, and are labeled with the approximated direct-P arrival delay time. Because of our focus on anisotropic structure of the mantle lithosphere, we focus on interpreting boundaries in anisotropy at delay times greater than the delay time of the Moho phase (as determined from the single-binned, radial component receiver functions shown in Figure 5).

The results of our harmonic decomposition for the Wyoming province stations (EGMT, K22A, and RSSD) are shown in Figure 6. We can make two simple initial observations for this group of stations: first, significant negative phase energy is present on the constant term (k=0) at MLD depths, indicating that the boundary requires an isotropic drop in velocity (or a change in radial anisotropy). Second, it is clear that both the proportion of energy distributed among the four non-constant expansion terms (k=1,2) and their arrival times vary between stations.

More specifically, the number of inferred anisotropic or dipping boundaries highlighted at each Wyoming Province station varies between two (RSSD) and five (EGMT) (recall that the boundaries are selected based on peaks in the summation of absolute amplitudes among the four non-constant components). Notably, there appears to be agreement between (isotropic) MLD delay times and anisotropic boundary delay times at each of the three stations, although we also infer the existence of anisotropic (and/or dipping) boundaries at delay times that are not associated with the MLD arrival. The amplitudes at EGMT are the largest (suggesting a strong influence from dipping or anisotropic structure), followed by RSSD. While evidence of anisotropy exists at K22A, the converted phase amplitudes appear substantially smaller, indicating weaker anisotropy and/or more gradual gradients. We observe no obvious correlations in the character of the *k*=1,2 expansion terms among the different stations. For example, EGMT and K22A have interfaces in anisotropy located at 7.2 s and 7.1 sec, respectively, but while both stations have a positive phase on the sin(2θ) component, and a negative on the cos(θ), the cos(2θ) and sin(θ) are approximately zero on K22A and negative/positive for station EGMT. Likewise, the boundary at 9.6 s for station EGMT has most energy contained on the sin(2θ) stack, while at 9.5 s at RSSD the largest amplitude phase is on the sin(θ) stack.

Harmonic stacking results for the three Superior Province stations are shown in Figure 7. Similar to the Wyoming Province, the Superior province stations show strong evidence for both an isotropic change in velocity associated with the MLD and anisotropic/dipping layering, with little consistency in the behavior of non-constant expansion term amplitudes between stations. For example, while we observe conversions from a boundary at 12.8 s at both stations AGMN and ECSD, the polarities for each of the two stations are opposite on the sin(2θ) component, positive on the cos(θ) component at station AGMN, to significantly positive at ECSD. The number of highlighted boundaries ranges from two (at station ULM) to five (at station AGMN). More generally, the converted phase amplitudes are similar among the different stations, although station AGMN appears to have more energy on the scattered/unmodeled portion of the decomposed results, suggesting the presence of heterogeneities. Station ULM has a notable lack of modeled energy below 90 km, with the exception of a phase arriving at 13.4 sec, which arrives within the same time window as the first crustal multiple (and thus may not be interpretable).

4.3. Detailed results at individual stations

The single-bin stacks shown in Figure 5, along with the harmonic decomposition results shown in Figures 5 and 6, give a general picture of our RF data and how lithospheric structure might vary laterally within our study region. In the following subsections, we describe in more detail the key features of our RF results for the six selected stations in the context of the local geologic and tectonic settings, along with our inferences on lithospheric structure beneath each station. While we do not discuss the results in detail for the remainder of the stations, RF data for those stations are shown in the supplemental materials. For each station discussed in this section, we show in Figures 7-12 radial and transverse component RFs as a function of backazimuth, along with radial component RFs as a function of epicentral distance, which can be used to check for possible moveout of later arrivals that may be indicative of multiply scattered phases.

4.3.1. EGMT, Wyoming Province

Station EGMT (Figure 8), located in north-central Montana, occupies the boundary between the Medicine Hat Block and the Great Falls Tectonic Zone (GFTZ), a tectonically active region (with recurrent movement since the Proterozoic) composed of northeast-trending, high-angle faults and shear zones [*O'Neill and Lopez,* 1985]. EGMT is also situated along the southern edge of the Bearpaw Mountains, a region of Laramide-associated, high-K volcanism [e.g., *MacDonald et al.,* 1992], with ages of 50-54 Ma [*Marvin et al.,* 1980].

The Moho phase at station EGMT arrives on the radial component RFs at a delay time of 5.3 s (~49 km) (Table 1). An additional positive arrival, likely corresponding to the bottom of a relatively thin (<1km) sedimentary sequence, is present at ~1 s delay time. Extensive negative phase energy is present on the radial component RFs (Figure 8), with a distinct trough at 7.6 s (~72 km) delay time, and a broad range of negative phase energy at ~11-17 s (~111-168 km). We interpret both of these negative arrivals as likely MLD phases, although it is possible that the latest arriving energy may correspond to the velocity drop at the LAB [*Foster et al.,* 2014]. Harmonic stacking results at this station (Figure 6) indicate the presence of multiple boundaries in anisotropy and/or dipping structure, at approximately 5.4, 7.3, 11.2, 14.2 and 16.1 seconds. These inferred boundaries manifest themselves directly in the transverse component RFs as energy arriving within these time ranges, with amplitudes and polarities that vary with backazimuth (Figure 8). There is some agreement between the arrival times of the anisotropic/dipping boundaries and of the MLDs (Figure 8a), although arrivals due to anisotropic or dipping boundaries are not confined exclusively to delay times associated with the MLDs. The most prominent polarity flip on the transverse component RFs is the one that occurs at 7.2 seconds, between 180-240 degrees back azimuth (Figure 8b; bottom panel). This boundary also appears prominently in the harmonic stack (Figure 6) at a relative (to 90 km) time of approximately -2.1 seconds. The presence of significant energy on the sin(2θ) component suggests that a contrast in azimuthal anisotropy is present.

4.3.2. K22A, Wyoming Province

K22A (Figure 9) is located in southern Wyoming, within the Archean craton. The station is situated on relatively thin sediment (<1 km [*Yeck et al.,* 2014]) outside the southeastern edge of the Wind River Basin [*Blackstone,* 1993], and to the northwest of the Laramie Mountains. Both the Wind River Basin and the Laramie Mountains are the result of Laramide-associated deformation.

The Moho phase at station K22A arrives relatively late (6.2 sec), corresponding to approximately 58 km depth (Figure 9). Using Ps H-k stacking, and taking into account effects of sedimentary reverberations, *Yeck et al.* [2014] found the depth to the Moho at K22A to be 54±5.5 km, consistent with our results. From the single-binned, radial component Ps receiver function (Figure 5) we find two distinct negative phases (interpreted as MLDs) at 8.0 s (~76 km) and 15.3 s (~150 km), although there is considerable negative phase energy scattered throughout the time range of 8-15 seconds (Figure 9). Harmonic stacking results for station K22A (Figure 6) show a dearth of coherent, large amplitude phases on the θ or 2θ components beneath the Moho, suggesting that this station does not overlie multiple strong contrasts in anisotropy within the lithosphere. However, we note that considerable energy is present on the cos(2θ) component near the Moho delay time, suggesting a contrast in azimuthal anisotropy across the Moho; this also manifests as a four-lobed pattern on the transverse component RFs (Figure 9b; bottom panel). Several small-amplitude phases, including arrivals at 12.9, 15.2 and 17.0 seconds, exhibit some evidence for anisotropic and/or dipping structure, but the weak arrivals suggests that any contrasts are not strong. Compared to other stations in the Wyoming and Superior Provinces, the relatively high amplitudes seen in the unmodeled portions of the harmonic stack (Figure 6) compared to other stations in the Wyoming and Superior provinces suggests a stronger degree of lateral heterogeneity beneath K22A.

4.3.3. RSSD, Wyoming Province

Located along the western flank of the Black Hills in South Dakota, station RSSD sits at the eastern edge of the Wyoming Province, near the Trans-Hudson orogen. While uncertainties exist in the timing and extent of deformation associated with the Trans-Hudson orogeny [*Dahl et al.,* 1999], the crystalline basement of the Black Hills is thought to consist of a north-trending zone of deformed, early Proterozoic continental margin material [*Hoffman,* 1989]. More recently, the Black Hills underwent deformation and uplift during the Laramide.

The Moho-converted phase at RSSD arrives on the radial component RFs at 5.7 s (~53 km) (Figure 10). Our estimate of Moho depth is greater than that estimated by the Earthscope Automated Receiver Survey (EARS) [*Crotwell and Owens,* 2005; *IRIS DMC,* 2010]; however, the H-k stacks at RSSD produce several local maxima, suggesting complex structure in the lower crust. Earlier results *by Zandt and Ammon* [1995] found that a range of crustal thicknesses from 46-52 km are compatible with the data. Negative phases observed at 9 s (~86 km) and 14.2 s (~139 km), are interpreted to be MLDs (Figure 10). Harmonic stacking results at RSSD (Figure 6) indicate the presence of multiple boundaries in anisotropy and/or dipping structure. Of the five most prominent boundaries, three (0.9 sec, 3.9 sec, and 5.2 sec) arrive before the Moho phase (Figure 6) and thus represent intracrustal structure. The phases associated with lithospheric structure arrive at 9.5 s and 12.8 sec; the first of these coincides with the earlier isotropic MLD arrival. Clear changes in transverse component RF polarity are evident at both delay times (Figure 10b; bottom panel). The boundary at 9.5 s exhibits evidence of contributions from both θ and 2θ components, while the boundary at 12.8 s appears to be dominated by the single θ expansion terms (Figure 6).

4.3.4. ECSD, Superior Province

Station ECSD is located in southeastern South Dakota, within the Superior Province, on top of the Sioux Quartzite. The Sioux Quartzite, described as a chemically (super)mature quartz arenite formed during the late Paleoproterozoic [e.g., *Medaris et al.,* 2003; *Whitmeyer and Karlstrom,* 2007] underlies four northwest-trending basins [*Southwick et al.,* 1986]. Based on the chemical maturity, the quartzite deposits have been interpreted as resulting from sedimentation on a passive continental margin in a tectonically stable setting. The quartzite rests noncomformably on Archean-aged Superior Province basement.

The Moho phase arrives at station ECSD at a delay time of 5.4 s (~50 km) and a single negative phase, observed at 13.8 s (~135 km), is interpreted as the MLD (Figure 11). A Moho depth estimate of 50 km from EARS is consistent with our results. In the harmonic stacks, three delay times are highlighted (7.5, 10.0, and 12.8 sec) at which considerable energy associated with anisotropy and/or dipping structure is present (Figure 7). These delay times are also highlighted in the transverse component RFs (Figure 11b; bottom panel). Each of the boundaries has energy expressed on the θ and 2θ harmonic expansion components. Overall, the unmodeled amplitudes are small, indicating that scattering due to heterogeneity is not a significant issue beneath this station (Figure 7). Notably, while we infer both an isotropic MLD and a number of anisotropic/dipping boundaries within the mantle lithosphere beneath ECSD, these boundaries are not co-located.

4.3.5. AGMN, Superior Province

Station AGMN is located within the Wabigoon subprovince, which is a middle to late Archean volcanic/plutonic terrane found in northwestern Minnesota and southern Manitoba [*Card,* 1990]. The Moho phase at AGMN arrives at 5.2 s (~47 km), similar to the EARS estimate of 49 km. Negative radial component phase arrivals at 10.8 (~105 km) and 16.1 (~158 km) are observed and interpreted to correspond to MLDs (Figure 12).

Harmonic stacking results for station AGMN are dominated by a large-amplitude phase on the cos(θ) component at approximately 8.0 s delay time (relative to the direct P arrival). Several smaller-amplitude phases at 5.8 sec, 10.8 sec, 12.8 s and 15.5 s appear to stack across the four non-constant harmonic expansion terms (Figure 7). Of these phases, two appear to arrive at or near the same times as the MLDs. In some instances, the amplitude of the unmodeled portion is equivalent to the amplitudes of the modeled results, suggesting scattering due to lateral heterogeneity. Clear evidence of polarity reversals is seen on the transverse component RFs (Figure 12b; bottom panel). For example, the transverse component arrival at 8.0 seconds changes from negative to positive polarity at 30-40 degrees back azimuth, and from positive to negative polarity at 175 to 180 (Figure 12b; bottom panel). We also observe a clear case of a four-lobed polarity flip, indicative of a contrast in azimuthal anisotropy, at 12.8 seconds.

4.3.6. ULM, Superior Province

Station ULM is located within the Wabigoon subprovince, as is station AGMN. The Moho phase arrival (Figure 13) at 3.9 s delay time (~35 km) agrees well with a previously estimated Moho depth from Ps receiver functions of 36±2 km [*Abt et al.,* 2010]. Two small-amplitude negative phases, interpreted as MLDs, are observed at delay times of 6.5 s (~61 km) and 8.6 s (~82 km) (Figure 13). These results are generally compatible with the Sp receiver function analysis of station ULM [*Abt et al.,* 2010], where a broad range of negative energy is observed from ~70 to 115 km, with a peak in negative energy at 101±14 km.

In addition to the Moho and MLD arrivals, harmonic stacking (Figure 7) indicates peaks in amplitude at 5.2 sec, 8.0 s and 13.4 s seconds. We disregard the peak at 13.4 s because of its arrival at the same delay time as that expected for the first crustal multiple, as illustrated by the epicentral distance bins in Figure 13a. The boundaries at 5.2 s and

8.0 s coincide with the timing of the MLD phases. There is some evidence of a polarity flip on the transverse component RFs at 125-130 degrees for the discontinuities at 5.2 seconds; interestingly, however, no evidence of a polarity flip is visible at 8 s (Figure 13b; bottom panel). According to the harmonic stacking (Figure 7), both discontinuities have energy expressed on the θ and 2θ expansion terms.

5. Discussion

5.1. Differentiating between dipping interfaces and dipping anisotropy

A limitation of the harmonic regression analysis in this study, and in the analysis of transverse component receiver functions more generally, is the difficulty in discriminating between dipping isotropic interfaces contrasts in anisotropy with a dipping axis of symmetry. Both of these scenarios produce a 2-lobed polarity pattern with backazimuth on transverse component RFs, which is modeled with a single θ harmonic expansion term. Subtle variations between the two mechanisms do exist, and were explored in some detail by *Levin and Park* [1997], who noted that the most reliable discriminant is the appearance of subtle differences in delay times as a function of back azimuth. Variations in amplitude with back azimuth are also theoretically present, but are considerably less reliable due to scattering. However, without detailed forward modeling for the specific dip geometry of the interface and anisotropy direction, it is difficult to predict expected delay time offsets and compare them to RF observations, and the data may not be able to uniquely discriminate between the two scenarios.

Another possible strategy for discriminating dipping interfaces from the presence of dipping anisotropy is to examine the transverse component for evidence of SH arrival energy at zero delay time due to the refraction of the direct P arrival. If energy is present (and mirrors the signal at greater delay times), it indicates the presence of a dipping isotropic interface [e.g., *Wirth and Long,* 2012]. At some of our stations, such as RSSD, we do see evidence for coherent SH particle motion at zero delay time on the transverse component (Figure 10b; bottom panel). However, a difficulty in interpreting this arrival is the fact that at all of our stations we have evidence for multiple discontinuities, and that some of these discontinuities arrive at or before the Moho phase. Again, without detailed forward modeling it is difficult to determine which of the discontinuities represents a dipping interface [e.g., *Shiomi and Park,* 2008; *Wirth and Long,* 2014]. Despite the ambiguity inherent in the interpretation of the k=1 terms of the harmonic expansion, the interpretation of the k=0 (corresponding to an apparently isotropic velocity contrast) and k=2 (corresponding to a contrast in azimuthal anisotropy) terms is much more straightforward, and we focus on these in our subsequent discussion.

5.2. Anisotropy and the mid-lithospheric discontinuity

Our results indicate that the mid-lithospheric discontinuities beneath the Wyoming and Superior provinces require a velocity drop that does not vary with direction, as evidenced by the large constant component (k=0) in the harmonic expansion at the relevant arrival times. Put another way, the harmonic decomposition results make it clear that a boundary in azimuthal anisotropy cannot by itself explain the negative phases on the radial component RFs at the stations examined in this study. The simplest explanation for the large negative phase at mid-lithospheric depths in our study is that the

MLDs represent isotropic drops in velocity. While it is true that at some stations we do infer a contrast in anisotropy at depth(s) similar to the isotropic MLDs, a contrast in azimuthal anisotropy alone cannot explain our radial component RF results, nor do we observe this correspondence for all inferred MLD interfaces.

Our inference that the MLD does not always and everywhere correspond to a contrast in azimuthal anisotropy beneath the Wyoming and Superior Provinces shares some similarities with previous studies of layered anisotropic structure in the mantle lithosphere beneath North America. Using similar analysis techniques to ours, *Wirth and Long* [2014] found that while there is an excellent correspondence in depth between the MLD and an inferred contrast in azimuthal anisotropy beneath the Granite-Rhyolite Province in the central United States, an isotropic velocity drop was required to fit the radial component RF observations. Likewise, tomographic imaging beneath North America suggests that a decrease in isotropic velocity at mid-lithospheric depths is required to fit the data [*Yuan et al.,* 2011], although these models also exhibit a contrast in azimuthal anisotropy in the mid-lithosphere.

What are the implications of our observations of multiple MLD arrivals that seem to require isotropic velocity drops within the lithosphere beneath our study area? While an isotropic velocity contrast at mid-lithospheric depths could be explained through thermally activated mechanisms such as anelastic grain boundary sliding [*Karato,* 2012; *Karato et al.,* 2015], it is unclear as to whether the predicted amplitudes are large enough to match real data [*Selway et al.,* 2015]. Detailed modeling of the velocity gradient at three stations directly south of our study area, but within a region exhibiting similar MLD characteristics (namely the presence multiple MLD phases), indicates that a drop of 6.5%

to 11% shear wave speed over 0 km depth is needed [*Hopper and Fischer*, 2015]. Such a gradient is unlikely to be explained with any other thermally activated mechanism. Instead, sharp changes in composition, possibly due to a layer(s) of frozen melt [e.g., *Ford et al.,* 2010; *Hopper and Fischer,* 2015] or a layer of volatile-rich amphibole [*Selway et al.,* 2015] or phlogopite [*Hansen et al.,* 2015] appear to represent a more plausible mechanism, and may be consistent with evidence from xenoliths for a hydrous mineral layer at mid-lithospheric depths [*Rader et al.,* 2015]. The presence of widespread Cenozoic aged volcanism throughout much of the western U.S., including locales such as the Bearpaw Mountains (station EGMT), also points to a potentially volatile rich mantle lithosphere, capable of producing a substantial drop in seismic velocity [*Hansen et al.,* 2015].

Another possible explanation, and one that we can only address indirectly, is that a boundary in radial anisotropy (that is, transverse isotropy with a vertical axis of symmetry, with no variations in velocity in the horizontal plane) is responsible for the apparent change in velocity at MLD depths. This mechanism has been proposed by others [e.g., *Rychert and Shearer,* 2009; *Ford,* 2013], but it still requires an argument for a widespread and consistent anisotropic geometry, despite the occurrence of regional tectonic events that can re-orient anisotropic fabrics [e.g., *Jung et al.,* 2006; *Selway et al.,* 2015]. While radial anisotropy is likely present within the North American lithosphere, there is no evidence for a pervasive boundary or boundaries at mid-lithospheric depths [e.g., *Nettles and Dziewonski,* 2008; *Yuan et al.,* 2011]. Furthermore, there appear to be large lateral variations in radial anisotropy within the Trans-Hudson orogeny [*Yuan et al.,* 2014] making an argument for widespread boundaries less likely.

5.3. Lateral variations in azimuthal anisotropy

This study presents evidence for multiple layers of azimuthal anisotropy within the mantle lithosphere beneath most stations in our study area. Our inference of significant lithospheric anisotropy is consistent with conclusions from comparisons between shear wave splitting and absolute plate motion in our study region, which seem to require a lithospheric contribution and indicate the presence of lateral variations [e.g., *Hongsresawat et al.,* 2015]; however, the RF technique used in this study can place much tighter constraints on the depth of anisotropy. In the presence of a single layer of anisotropy juxtaposed next to an isotropic interface, we would be able to use the variations in back azimuthal distribution to infer anisotropy orientation without detailed forward modeling, since the relationship between fast axis direction and results are clear (Figure 3). However, the presence of multiple anisotropic and/or dipping interfaces yields significantly more complicated results. Figure 14 presents a handful of cases in which two layers of varying anisotropic orientation are vertically juxtaposed. The resulting variations in phase amplitude and timing deviate from the simple θ and 2θ patterns presented in Figure 3 and more closely replicate the complexity observed in our results, where most of the interfaces appeared to exhibit evidence for contributions from both the θ and 2θ terms.

Our results also demonstrate that the depth and geometry of the anisotropic interfaces vary regionally, with striking differences in anisotropic structure among individual stations. This observation is perhaps most clearly demonstrated in the summary of our results shown in Figure 15, which shows our stations ordered from west (left) to east (right). We show a rose plot for each interface at which we infer a contrast in anisotropy, illustrating the variations in transverse component RF amplitude and polarity as a function of backazimuth, along with a model of the variations derived from the harmonic decomposition results. Regardless of whether we compare these rose plots for a given delay time (e.g., all interfaces between 7 and 8 seconds), or at the times associated with the isotropic MLD (gray boxes in Figure 15, ±0.5 seconds), we see little evidence for similarities in anisotropic (and/or dipping structure) signature among different stations. Rather, the comparisons in Figure 15 make it clear that layered anisotropic structure in the mantle lithosphere exhibits significant lateral variations within and between the Wyoming and Superior Provinces.

This aspect of our conclusions contrasts with previous inferences of the geometry of lithospheric anisotropy (and its lateral variability) beneath continental North America. Specifically, *Yuan and Romanowicz* [2010] suggested the presence of a continent-wide anisotropic boundary in the mid-lithosphere based on the joint inversion of *SKS* splitting and surface wave dispersion. One potential reason for this apparent discrepancy may be the differences in sensitivity between methods. While receiver function analysis is capable of imaging sharp gradients, it is insensitive to gradual changes, which are better characterized with surface wave tomography.

A comparison of our results to those obtained using similar analysis techniques elsewhere show areas of agreement as well as contrast. *Schulte-Pelkum and Mahan* [2014] performed an analysis similar to the one described in our study, and mapped amplitudes and directions for the θ component (referred to as degree-1 signal) and 2θ component (referred to as degree-2 signal) across the United States at crustal depths. In their analysis, both θ and 2θ components are present to varying degrees, and exhibit regional dependence. Overall, the coherence between stations in a given region are larger than what we observe, but that may be due to their denser sampling, as well as the focus on crustal structure. At four long-running stations located within the Proterozoic Granite-Rhyolite province of North America, *Wirth and Long* [2014] uncovered a consistent contrast in anisotropy at mid-lithospheric depths with similar geometry (consistent with a north to northwest trending axis of horizontal symmetry in the upper mantle lithosphere). This observation supports a model of fabric development tied to a series of subduction or underthrusting-type events, similar to those inferred in the Canadian Shield [e.g., *Bostock,* 1998; *Mercier et al.,* 2008; *Snyder,* 2008]. Given the history of the Wyoming and Superior cratons, it is possible that anisotropy observed in this study results in part from similar processes, but the lack of widespread, regionally coherent anisotropic layering contrasts with the structure observed beneath the Granite-Rhyolite province. Without performing detailed forward modeling for each individual station we cannot characterize the orientation of anisotropy in each layer, but such modeling represents an important target for future work.

We can suggest three possible explanations for the difference in regional coherence between our results and those of *Wirth and Long* [2014] for the Granite-Rhyolite province. The first possibility is that the region sampled by our study is significantly larger than that of *Wirth and Long* [2014], increasing the probability of imaging variations in lateral structure. Another possibility is that the anisotropic structure of the mantle lithosphere associated with the formation of the Archean Wyoming and Superior cratons was modified by subsequent tectonic activity, particularly the Laramide

Orogeny between 40-70 Ma. Widespread Laramide-associated lithospheric deformation – and possible modification of anisotropic structure, including reorientation of the fast axis, is plausible, given the evidence for lithospheric anisotropy associated with past orogenesis elsewhere in North America [e.g., the Appalachians; *Long et al.,* 2016]. A third possible, if more speculative, explanation is that the processes associated with the formation of the Wyoming and Superior Cratons in the Archean differed from those operating in the Proterozoic, when the Granite-Rhyolite province was formed (along with other elements that today make up the core of continental North America). Differentiating among these possibilities will require detailed forward modeling of the individual station results, which will likely require the use of model space search approaches [e.g., *Wirth et al.,* in revision] and is beyond the scope of this observational study. However, such modeling would likely lend insight into the anisotropic character of the lithosphere and the deformation processes responsible for producing such a complex mantle fabric and will be the focus of future efforts in the region.

6. Summary

We have presented anisotropic Ps receiver function analysis for a set of 13 long-running stations in the Wyoming and Superior Provinces, and provided a detailed interpretation for a subset of six stations with the highest-quality data. Our results show evidence for significant complexity within the mantle lithosphere of the Wyoming and Superior Provinces and immediate surrounding areas. The application of the harmonic regression analysis technique to radial and transverse component RFs, binned as a function of backazimuth, allows us to isolate and identify contributions from apparently isotropic velocity contrasts, dipping interfaces and/or dipping anisotropy, and contrasts in azimuthal anisotropy with depth. Our data do not support a model in which the MLD corresponds exactly to a sharp contrast in azimuthal anisotropy. Instead, beneath most stations our data require multiple (apparently) isotropic decreases in velocity with depth at depths internal to the lithosphere. The explanation for these discontinuities remains elusive, although our data appear to be most consistent with boundaries in composition within the lithosphere. In addition to requiring the presence of isotropic MLDs, our transverse component RF data indicate the presence of multiple layers of anisotropy in the mantle lithosphere beneath most stations. We find little evidence of regional consistency in inferred anisotropic structure among stations within, or across, adjacent Archean provinces. Instead, our results indicate a strongly heterogeneous mantle lithosphere with large lateral variations in azimuthal anisotropy, likely due to differences in deformation history. Future work will include detailed forward modeling of individual station results, allowing us to constrain the precise geometry of individual anisotropic layers.

7. Acknowledgements

This work was supported by NSF grant EAR-1358325. Data from the CN, TA, and US seismic networks were accessed via the IRIS Data Management Center (DMC). We thank Jeff Park for helpful discussions regarding methodology, editor Martha Savage, and two anonymous reviewers for the constructive comments that helped to improve this paper

8. References

Abt, D. L., K. M. Fischer, S. W. French, H. A. Ford, H. Yuan, and B. Romanowicz (2010), North American lithospheric discontinuity structure imaged by Ps and Sp receiver functions, J. Geophys. Res., 115, B09301, doi:10.1029/2009JB006914.

Allmendinger, R.W., J. A. Brewer, L. D. Brown, J. E. Oliver, and S. Kaufman (1982), COCORP profiling across the Rocky Mountain front in southern Wyoming, Part II: Precambrian basement structure and its influence on Laramide deformation, Geol. Soc. Am. Bull. 93, 1253-1263.

Bianchi, I., J. Park, N. Piana Agostinetti, and V. Levin (2010), Mapping seismic anisotropy using harmonic decomposition of receiver functions: An application to Northern Apennines, Italy, J. Geophys. Res., 115, B12317, doi:10.1029/2009JB007061.

Bird, P. (1984), Laramide crustal thickening event in the Rocky Mountain foreland and Great Plains. *Tectonics*, *3*, 741-758.

Blackstone, D. (1993), Precambrian basement map of Wyoming: Outcrop and structural configuration, Geol. Soc. Am. Spec. Pap., 280, 335–338, doi:10.1130/SPE280-p335.

Bodin, T., H. Yuan, and B. Romanowicz (2013), Inversion of receiver functions without deconvolution—Application to the Indian craton, Geophys. J. Int., 196, 1025–1033, doi:10.1093/gji/ggt431.

Boerner, D. E., J. A. Craven, R. D. Kurtz, G. M. Ross, and F. W. Jones (1998), The Great Falls Tectonic Zone: Suture or intracontinental shear zone?, Can. J. Earth Sci., 35, 175–183, doi:10.1139/e97-104.

Bostock, M. G. (1998), Mantle stratigraphy and evolution of the Slave province, J. Geophys. Res., 103, 21183–21200, doi:10.1029/98JB01069.

Brewer, J.A., S. B. Smithson, J. E. Oliver, S. Kaufman, and L. D. Brown (1980), The Laramide Orogeny: Evidence from COCORP Deep Crustal Seismic Reflection Profiles in the Wind River Mountains, Wyoming, Tectonophysics, 62, 165-189.

Card, K. D. (1990). A review of the Superior Province of the Canadian Shield, a product of Archean accretion. Precambrian Res., 48, 99-156, doi:10.1016/0301-9268(90)90059-Y

Chen, C. W., S. Rondenay, R. L. Evans, and D. B. Snyder (2009), Geophysical detection of relict metasomatism from an Archean (3.5 Ga) subduction zone, Science, 326, 1089–1091, doi:10.1126/science.1178477.

Chu, R., B. Schmandt, and D. V. Helmberger (2012), Upper mantle *P* velocity structure beneath the Midwestern United States derived from triplicated waveforms, Geochem. Geophys. Geosyst., 13, Q0AK04, doi:10.1029/2011GC003818.

Collins, J. A., F. L. Vernon, J. A. Orcutt, R. A. Stephen (2002), Upper mantle structure beneath the Hawaiian swell: constraints from the ocean seismic network pilot experiment. Geophys. Res. Lett. 29, 1522. doi:10.1029/2001GL013302.

Cooper, C. M., and M. S. Miller (2014), Craton formation: Internal structure inherited from closing of the early oceans: Lithosphere, v. 6, p. 35–42, doi:10.1130 /L321.1.

Cross, T. A., & Pilger, R. H. (1978), Tectonic controls of Late Cretaceous sedimentation, western interior, USA. Nature, 274, 653 – 657, doi:10.1038/274653a0

Crotwell, H. P., and T. J. Owens (2005), Automated receiver function processing, Seismol. Res. Lett., 76, 702–709, doi:10.1785/gssrl.76.6.702.

Dahl, P. S., D. K. Holm, E. T. Gardner, F. A. Hubacher, and K. A. Foland (1999), New constraints on the timing of Early Proterozoic tectonism in the Black Hills (South Dakota), with implications for docking of the Wyoming province with Laurentia, Geol. Soc. Am. Bull., 111, 1335-1349.

Dickinson, W. R. (1978), Plate tectonics of the Laramide orogeny, GSA Memoirs, 151, 355-366, doi:10.1130/MEM151

Ducker, K., Yuan, H., and Zurek, B. (2001), Thick-structured Proterozoic lithosphere of the Rocky Mountain region. *GSA Today*, *11*, 4-9.

Eaton, D. W., G. M. Ross, and R. M. Clowes (1999), Seismic-reflection and potential-field studies of the Vulcan structure, western Canada: A Paleoproterozoic Pyrenees?, J. Geophys. Res., 104(B10), 23255–23269, doi:10.1029/1999JB900204.

Eckhardt, C. and W. Rabbel (2011), P-receiver functions of anisotropic continental crust: a hierarchic catalogue of crustal models and azimuthal waveform patterns, Geophys. J Int., 187, 439–479.

French, S., V. Lekic, and B. Romanowicz (2013), Waveform tomography reveals channeled flow at the base of the oceanic asthenosphere, Science, 342, 227-230.

Fischer, K. M., H. A. Ford, D. L. Abt, and C. A. Rychert (2010), The lithosphere-asthenosphere boundary, Annu. Rev. Earth Planet. Sci., 38, 551–575, doi:10.1146/annurev-earth-040809-152438.

Ford, H. A., K. M. Fischer, D. L. Abt, C. A. Rychert, and L. T. Elkins-Tanton (2010), The lithosphere–asthenosphere boundary and cratonic lithospheric layering beneath Australia from Sp wave imaging, Earth Planet. Sci. Lett., 300, 299–310, doi:10.1016/j.epsl.2010.10.007.

Ford, H. A., K. M. Fischer, and V. Lekic (2014), Localized shear in the deep lithosphere beneath the San Andreas fault system, Geology, 42, 295-298.

Foster, K., K. Dueker, B. Schmandt, and H. Yuan (2014), A sharp cratonic lithosphere–asthenosphere boundary beneath the American Midwest and its relation to mantle flow, Earth Planet. Sci. Lett., 402, 82–89, doi:10.1016/j.epsl.2013.11.018.

Fouch, M. J., and S. Rondenay (2006), Seismic anisotropy beneath stable continental interiors. Phys. Earth Planet. Int., 158, 292-320.

Frederiksen, A. W. and M. G. Bostock (2000), Modelling teleseismic waves in dipping anisotropic structures. Geophys. J. Int. 141, 401-412.

Frost, C. D., B. R. Frost, K. R. Chamberlain and T. P. Hulsebosch (1998), The Late Archean history of the Wyoming province as recorded by granitic magmatism in the Wind River Range, Wyoming. Precambrian Res., 89(3), 145-173.

Griffin, W. L., S. Y. O'Reilly and C. G. Ryan (1999), The composition and origin of sub-continental lithospheric mantle. In Mantle petrology: field observations and high-pressure experimentation: a tribute to Francis R.(Joe) Boyd (Vol. 6, pp. 13-45). The Geochemical Society Houston.

Hall, D. H., and W. C. Brisbin (1982), Overview of regional geophysical studies in Manitoba and northwestern Ontario. Can. J. Earth Sci.,19(11), 2049-2059.

Hansen, S., and K. Dueker (2009), P-and S-wave receiver function images of crustal imbrication beneath the Cheyenne Belt in southeast Wyoming, Bull. Seismol. Soc.

Am., 99, 1953–1961, doi:10.1785/0120080168.

Hansen, S. M., K. G. Dueker, J. C. Stachnik, R. C. Aster, and K. E. Karlstrom (2013), A rootless rockies—Support and lithospheric structure of the Colorado Rocky Mountains inferred from CREST and TA seismic data, Geochem. Geophys. Geosyst., 14, 2670–2695, doi:10.1002/ggge.20143.

Hansen, S. M., Dueker, K., & Schmandt, B. (2015), Thermal classification of lithospheric discontinuities beneath USArray. *Earth Planet. Sci. Lett.*, 431, 36-47, doi:10.1016/j.epsl.2015.09.009.

Heit, B., F. Sodoudi, X. Yuan, M. Bianchi and R. Kind (2007), An S receiver function analysis of the lithospheric structure in South America. Geophys. Res. Lett. 34, L14307. doi:10.1029/2007GL030317.

Helffrich, G. (2006), Extended-time multitaper frequency domain cross-correlation receiver-function estimation. Bull. Seism. Soc. Am., 96(1), 344-347.

Hoffman, P. F. (1988), United Plates of America, the birth of a craton-Early Proterozoic assembly and growth of Laurentia, Annu. Rev. Earth Planet. Sci., 16, 543–603.

Hopper, E., H. A. Ford, K. M. Fischer, V. Lekic, and M. J. Fouch (2014), The lithosphere–asthenosphere boundary and the tectonic and magmatic history of the northwestern United States, Earth Planet. Sci. Lett., 402, 69–81, doi:10.1016/j.epsl.2013.12.016.

James, D. E., F. R. Boyd, D. Schutt, D. R. Bell, and R. W. Carlson (2004), Xenolith constraints on seismic velocities in the upper mantle beneath southern Africa, Geochem. Geophys. Geosyst., 5, Q01002, doi:10.1029/2003GC000551.

Jordan, T. H. (1978). Composition and development of the continental tectosphere. Nature, 274(5671), 544-548.

Karato, S. I. (2012), On the origin of the asthenosphere, Earth Planet. Sci. Lett., 321, 95–103, doi:10.1016/j.epsl.2012.01.001.

Karato, S. I., T. Olugboji, and J. Park (2015), Mechanisms and geologic significance of the mid-lithosphere discontinuity in the continents, Nat. Geosci., 8, 509–514, doi:10.1038/ngeo2462.

Kennett, B. L. N., E. R. Engdahl and R. Buland (1995), Constraints on seismic velocities in the Earth from traveltimes, Geophys. J. Int., 122(1), 108-124.

Kind, R., X. Yuan, and P. Kumar (2012), Seismic receiver functions and the lithosphere–asthenosphere boundary, Tectonophysics, 536, 25–43, doi:10.1016/j.tecto.2012.03.005.

King, S. D. (2005), Archean cratons and mantle dynamics. Earth Planet. Sci. Lett., 234(1), 1-14.

Kumar, P., X. H. Yuan, M. R. Kumar, R. Kind, X. Q. Li and R. K. Chadha, (2007), The rapid drift of the Indian tectonic plate. Nature, 449, 894–897.

Kumar, P., R. Kind, X. Yuan, and J. Mechie (2012), USArray receiver function images of the lithosphere-asthenosphere boundary, Seismol. Res. Lett., 83(3), 486–491, doi:10.1785/gssrl.83.3.486.

Kustowski, B., G. Ekström, and A. M. Dziewonski (2008), Anisotropic shear-wave velocity structure of the Earth's mantle: A global model, J. Geophys. Res., 113, B06306, doi:10.1029/2007JB005169.

Langston, 1979. Structure under Mount Ranier, Washington, inferred from teleseismic body waves. J. Geophys. Res., 84, 4749-4762 doi:10.1029/JB084iB09p04749.

Lee, C. T. A. (2006), Geochemical/petrologic constraints on the origin of cratonic mantle, Archean geodynamics and environments, 89-114.

Lekic, V., French, S. W., and K. M. Fischer (2011), Lithospheric thinning beneath rifted regions of southern California, Science, 334, 783-787, doi: 10.1126/science.1208898.

Lekic, V., and K. M. Fischer (2014), Contrasting lithospheric signatures across the western United States revealed by Sp receiver functions, Earth Planet. Sci. Lett., 402, 90–98, doi:10.1016/j.epsl.2013.11.026.

Lenardic, A., and L.-N. Moresi (1999), Some thoughts on the stability of cratonic lithosphere: Effects of buoyancy and viscosity, J. Geophys. Res., 104(B6), 12747–12758, doi:10.1029/1999JB900035.

Levin, V. and J. Park (1997), P□SH conversions in a flat□layered medium with anisotropy o arbitrary orientation. Geophy. J. Int. 131, 253-266.

Levin, V. and J. Park (1998) P-SH conversions in layered media with hexagonally symmetric anisotropy: a cookbook, Pure Appl. Geophys., 151, 669-697.

Li, X., R. Kind, K. Priestley, S. V. Sobolev, F. Tilmann, X. Yuan and M. Weber (2000), Mapping the Hawaiian plume conduit with converted seismic waves, Nature, 405, 938–941.

Li, X., X. Yuan and R. Kind (2007), The lithosphere–asthenosphere boundary beneath the western United States, Geophys. J. Int. 170, 700–710.

Liu, Z., J. Park and D. M. Rye (2015), Crustal anisotropy in northeastern Tibetan Plateau inferred from receiver functions: Rock textures caused by metamorphic fluids and lower crust flow?, Tectonophysics, 661, 66-80.

Macdonald, R., B. G. J. Upton, K D. Collerson, B. H. Hearn and D. James (1992), Potassic mafic lavas of the Bearpaw Mountains, Montana: mineralogy, chemistry, and origin. J. Petrol., 33(2), 305-346.

Marvin, R. F., B. C. Hearn, H. H. Mehnert, C. W. Naeser, R. E. Zartman and D. A. Lindsey (1980), Late Cretaceous–Paleocene–Eocene igneous activity in north-central Montana, Isochron-West, 29(3), 5-25.

Maupin, V., and J. Park (2007), Theory and observations: Wave propagation in anisotropic media, in Treatise on Geophysics, Volume 1, Seismology and Structure of the Earth, B. Romanowicz and A. Dziewonski, eds, Elsevier, Amsterdam, 289-321.

Medaris Jr, L. G., B. S. Singer, R. H. Dott Jr, A. Naymark, C. M. Johnson, and R. C. Schott (2003), Late Paleoproterozoic climate, tectonics, and metamorphism in the southern Lake Superior region and Proto–North America: evidence from Baraboo interval quartzites. J. Geol.,111(3), 243-257.

Mercier, J.-P., M. G. Bostock, P. Audet, J. B. Gaherty, E. J. Garnero, and J. Revenaugh (2008), The teleseismic signature of fossil subduction: Northwestern Canada, J. Geophys. Res., 113, B04308, doi:10.1029/2007JB005127.

Miller, M. S., and D. W. Eaton (2010), Formation of cratonic mantle keels by arc accretion: Evidence from S receiver functions, Geophys. Res. Lett., 37, L18305, doi:10.1029/2010GL044366.

Moulik, P., and G. Ekström (2014), An anisotropic shear velocity model of the Earth's mantle using normal modes, body waves, surface waves and long-period waveforms, Geophys. J. Intl., 199(3), 1713-1738.

Mueller, P. A., R. D. Shuster, J. L. Wooden, E. A. Erslev, and D. R. Bowes (1993), Age and composition of Archean crystalline rocks from the southern Madison Range, Montana: implications for crustal evolution in the Wyoming craton. Geol. Soc. Am. Bull., 105(4), 437-446.

Musacchio, G., D. J. White, I. Asudeh, and C. J. Thomson (2004), Lithospheric structure and composition of the Archean western Superior Province from seismic refraction/wide-angle reflection and gravity modeling, J. Geophys. Res., 109, B03304, doi:10.1029/2003JB002427.

Nettles, M., and A. M. Dziewoński (2008), Radially anisotropic shear velocity structure of the upper mantle globally and beneath North America, J. Geophys. Res., 113, B02303, doi:10.1029/2006JB004819.

Nikulin, A., V. Levin, and J. Park (2009), Receiver function study of the Cascadia megathrust: Evidence for localized serpentinization. Geochem. Geophys. Geosyst., 10, Q07004, doi:10.1029/2009GC002376

O'Neill, J. M., and D. A. Lopez (1985), Character and regional significance of Great Falls tectonic zone, east-central Idaho and west-central Montana. AAPG Bull., 69(3), 437-447.

Oreshin, S., L. Vinnik, D. Peregoudov and S. Roecker (2002), Lithosphere and asthenosphere of the Tien Shan imaged by S receiver functions. Geophys. Res. Lett. 29, 1191. doi:10.1029/2001GL014441.

Ozacar, A., H. Gilbert and G. Zandt, G (2008), Upper mantle discontinuity structure beneath East Anatolian Plateau (Turkey) from receiver functions, Earth Planet. Sci. Lett. 269, 426–434.

Ozacar, A. and G. Zandt (2009), Crustal structure and seismic anisotropy near the San Andreas Fault at Parkfield, California, Geophys. J. Int. 178, 1098-1104.

Park, J., H. Yuan, and V. Levin (2004), Subduction zone anisotropy beneath Corvallis, Oregon: A serpentinite skid mark of trench-parallel terrane migration? J. Geophys. Res., 109, B10306, doi:10.1029/2003JB002718.

Percival, J. A., M. Sanborn-Barrie, T. Skulski, G. M. Stott, H. Helmstaedt and D. J. White (2006), Tectonic evolution of the western Superior Province from NATMAP and Lithoprobe studies. Can. J. Earth Sci., 43(7), 1085-1117.

Porritt, R. W., M. S. Miller, and F. A. Darbyshire (2015), Lithospheric architecture beneath Hudson Bay, Geochem. Geophys. Geosyst., 16, 2262–2275, doi:10.1002/2015GC005845.

Porter, R., Y. Liu, and W. E. Holt (2016), Lithospheric records of orogeny within the continental U.S.,Geophys. Res. Lett., 43, 144–153, doi:10.1002/2015GL066950.

Porter, R., G. Zandt and N. McQuarrie (2011), Pervasive lower-crustal seismic anisotropy in Southern California: Evidence for underplated schists and active tectonics. Lithosphere, 3(3), 201-220.

Ritsema, J., A. Deuss, H. J. Van Heijst and J. H. Woodhouse (2011), S40RTS: a degree-40 shear-velocity model for the mantle from new Rayleigh wave dispersion, teleseismic traveltime and normal-mode splitting function measurements. Geophys. J. Int., 184(3), 1223-1236.

Rondenay, S. (2009), Upper mantle imaging with array recordings of converted and scattered teleseismic waves, Surv. Geophys., 30(4-5), 377-405.

Rychert, C.A., K. M. Fischer and S. Rondenay (2005), A sharp lithosphere–asthenosphere boundary imaged beneath eastern North America, Nature 436, 542–545.

Rychert, C. A., and P. M. Shearer (2009), A global view of the lithosphere-asthenosphere boundary, Science, 324(5926), 495–498, doi:10.1126/science.1169754.

Savage, M. K. (1998), Lower crustal anisotropy or dipping boundaries? Effects of receiver functions and a case study in New Zealand. J. Geophys. Res., 103, 15069-15.

Savage, M. K. (1999), Seismic anisotropy and mantle deformation: what have we learned from shear wave splitting?, Rev. Geophys., 37(1), 65-106.

Schaeffer, A. J., and S. Lebedev (2014), Imaging the North American continent using waveform inversion of global and USArray data, Earth Planet. Sci. Lett., 402, 26-41.

Schulte-Pelkum, V., & Mahan, K. H. (2014). A method for mapping crustal deformation and anisotropy with receiver functions and first results from USArray. *Earth Planet. Sci. Lett.*, 402, 221-233, doi:10.1016/j.epsl.2014.01.050

Schulte-Pelkum, V., G. Monsalve, A. Sheehan, M. R. Pandey, S. Sapkota, R. Bilham, and F. Wu (2005), Imaging the Indian subcontinent beneath the Himalaya, Nature, 435(7046), 1222-1225.

Selway, K., H. Ford, and P. Kelemen (2015), The seismic mid-lithosphere discontinuity, Earth Planet. Sci. Lett., 414, 45–57, doi:10.1016/j.epsl.2014.12.029.

Shapiro, S. S., B. H. Hager, T. H. Jordan (1999), Stability and dynamics of the continental tectosphere, Lithos, 48(1), 115-133.

Shiomi, K., and J. Park (2008), Structural features of the subducting slab beneath the Kii Peninsula, central Japan: Seismic evidence of slab segmentation, dehydration, and anisotropy, J. Geophys. Res.,113, B10318, doi:10.1029/2007JB005535.

Simons, F. J. and R. D. Van der Hilst (2003), Seismic and mechanical anisotropy and the past and present deformation of the Australian lithosphere, Earth Planet. Sci. Lett., 211, 271-286.

Simmons, N. A., A. M. Forte, L. Boschi, and S. P. Grand (2010), GyPSuM: A joint tomographic model of mantle density and seismic wave speeds, J. Geophys. Res., 115, B12310, doi:10.1029/2010JB007631.

Silver, P. G. (1996), Seismic anisotropy beneath the continents: probing the depths of geology, Ann. Rev. Earth Planet. Sci., 24, 385-432.

Silver, P. G., M. J. Fouch, S. S. Gao and M. Schmitz (2004), Seismic anisotropy, mantle fabric, and the magmatic evolution of Precambrian southern Africa, S. Afr. J. Geo., 107(1-2), 45-58.

Smithson, S. B., J. A. Brewer, S. Kaufman, J. E. Oliver, and C. A. Hurich (1979), Structure of the Laramide Wind River Uplift, Wyoming, from Cocorp deep reflection data and from gravity data, J. Geophys. Res., 84(B11),5955–5972, doi:10.1029/JB084iB11p05955.

Snelson, C. M., T. J. Henstock, G. R. Keller, K. C. Miller, and A. Levander (1998), Crustal and uppermost mantle structure along the Deep Probe seismic profile, Rocky Mt Geol., 33, 181–198.

Snyder, D. B. (2008), Stacked uppermost mantle layers within the Slave craton of NW Canada as defined by anisotropic seismic discontinuities. Tectonics, 27, TC4006.

Sodoudi, F., X. Yuan, Q. Liu, R. Kind and J. Chen (2006), Lithospheric thickness beneath the Dabie Shan, central eastern China from S receiver functions. Geophys. J. Int. 166, 1363–1367.

Sodoudi, F., X. Yuan, R. Kind, S. Lebedev, J. M. C. Adam, E. K€astle, and F. Tilmann (2013), Seismic evidence for stratification in composition and anisotropic fabric within the thick lithosphere of Kalahari Craton, Geochem. Geophys. Geosyst., 14, 5393–5412, doi:10.1002/2013GC004955.

Song, T.-R. A., and Y. Kim (2012), Localized seismic anisotropy associated with long-term slow-slip events beneath southern Mexico, Geophys. Res. Lett., 39, L09308, doi:10.1029/2012GL051324.

Southwick, D. L., G. B. Morey and J. H. Mossler (1986), Fluvial origin of the lower Proterozoic Sioux Quartzite, southwestern Minnesota, Geol. Soc. Am. Bull., 97(12), 1432-1441.

Thybo, H. (2006), The heterogeneous upper mantle low velocity zone, Tectonophysics, 416(1), 53–79, doi:10.1016/j.tecto.2005.11.021.

Van Schmus, W. R. and W. J. Hinze (1985), The midcontinent rift system. Ann. Rev. Earth Planet. Sci., 13, 345.

Vinnik, L., Kurnik, E., Farra, V., 2005. Lehmann discontinuity beneath North America: no role for seismic anisotropy. Geophys. Res. Lett. 32, L09306. doi:10.1029/ 2004GL022333.

Whitmeyer, S. J., and K. E. Karlstrom (2007), Tectonic model for the Proterozoic growth of North America, Geosphere, 3(4), 220–259, doi:10.1130/GES00055.1.

Wirth, E. A., and M. D. Long (2012), Multiple layers of seismic anisotropy and a low-velocity region in the mantle wedge beneath Japan: Evidence from teleseismic receiver functions, Geochem. Geophys. Geosyst., 13, Q08005, doi:10.1029/2012GC004180.

Wirth, E. A., and M. D. Long (2014), A contrast in anisotropy across mid-lithospheric discontinuities beneath the central United States—A relic of craton formation, Geology, 42(10), 851–854, doi:10.1130/G35804.1.

Wirth, E. A., M. D. Long, and J. Moriarty (in revision), A Markov chain Monte Carlo with Gibbs sampling approach to receiver function forward modeling, Geophys. J. Int., in revision.

Wittlinger, G., and V. Farra (2007), Converted waves reveal a thick and layered tectosphere beneath the Kalahari super-craton, Earth Planet. Sci. Lett., 254(3), 404–415, doi:10.1016/j.epsl.2006.11.048.

W€olbern, I., G. R€umpker, K. Link, and F. Sodoudi (2012), Melt infiltration of the lower lithosphere beneath the Tanzania craton and the Albertine rift inferred from S receiver functions, Geochem. Geophys. Geosyst., 13, Q0AK08, doi:10.1029/2012GC004167.

Yeck, W. L., A. F. Sheehan, M. L. Anderson, E. A. Erslev, K. C. Miller, and C. S. Siddoway (2014), Structure of the Bighorn Mountain region, Wyoming, from teleseismic receiver function analysis: Implications for the kinematics of Laramide shortening, J. Geophys. Res. Solid Earth, 119,7028–7042, doi:10.1002/2013JB010769.

Yuan, H., and B. Romanowicz (2010), Lithospheric layering in the North American craton, Nature, 466(7310), 1063–1068, doi:10.1038/nature09332.

Yuan, H., B. Romanowicz, K. M. Fischer, and D. Abt (2011), 3-D shear wave radially and azimuthally anisotropic velocity model of the North American upper mantle, Geophys. J. Int., 184(3), 1237–1260, doi:10.1111/j.1365-246X.2010.04901.x.

Yuan, H., and V. Levin (2014), Stratified seismic anisotropy and the lithosphere-asthenosphere boundary beneath eastern North America, J. Geophys. Res. Solid Earth, 119, 3096–3114, doi:10.1002/2013JB010785.

Zandt, G., and C. J. Ammon (1995), Continental crust composition constrained by measurements of crustal Poisson's ratio, Nature, 374(6518), 152-154.

9. Figures

Figure 1. Overview of major tectonic features within the study area. The base map is a simplified version of Archean and Proterozoic-aged basement features, modified from *Whitmeyer and Karlstrom* [2007]. The thirteen stations for which Ps receiver functions were calculated are marked according to network: US (inverted triangle), TA (square) and CN (circle). Gray-filled station markers indicate that the results are included in Figure 5.

Figure 2. Distribution of events (red circles) used to calculate Ps receiver functions for station RSSD (US). A total of 898 events from epicentral distances of 30°–100° were used.

Figure 3. (A) Cartoon drawings of models used to compute synthetic receiver functions

shown in (B) and synthetic harmonic stacks in (C). Cases 1 and 2 (left and center) have the same average velocity in the anisotropic layer as the layer in case 3 (right). (B) Radial (top) and transverse (bottom) component Ps receiver functions, binned as a function of back azimuth. (C) Top panel correspond to the modeled portion of the harmonic expansion. The bottom panel corresponds to the portion of the Ps receiver functions that cannot be modeled by the harmonic expansion.

Figure 4. Summary of different stacking and plotting conventions for station RSSD. (A) Single station stacked, radial component Ps receiver function. The Moho pick is shown in cyan and the MLDs are shown in magenta. (B) Radial (top) and transverse (bottom) component receiver functions binned as a function of back azimuth. Grey lines correspond to anisotropic interfaces selected from the harmonic regression in (C). (C) Top panel correspond to the modeled portion of the harmonic expansion. The bottom panel corresponds to the portion of the Ps receiver function that cannot be modeled by the harmonic expansion. Receiver functions are plotted as a function of delay time relative to the theoretical arrival time for an interface at 90 km depth (assuming the AK135 background velocity model). The 90 km and 0 km marks are drawn as horizontal black lines in all panels. (D) Transverse component Ps receiver function rose plots for inferred anisotropic boundaries.

Figure 5. Station-stacked, radial component Ps receiver functions shown in order from west (left) to east (right). Y-axis is delay time (relative to direct-P arrival) in seconds. Blue phases indicate positive amplitudes and correspond to a velocity increase with

depth; red indicates negative amplitudes corresponding to a velocity decrease with depth. Station names are shown along the top of the profile. The Moho picks (cyan) and negative picks interpreted as MLDs (magenta) are shown and correspond to the delay times listed in Table 1.

Figure 6. Ps receiver functions binned as a function of harmonic expansion terms for Wyoming Province stations EGMT, K22A and RSSD. Top panels correspond to the modeled portion of the harmonic expansion. The bottom panels correspond to the portion of the Ps receiver functions which cannot be modeled by the harmonic expansion. Both the modeled (Top panels) and unmodeled (Bottom panels) receiver functions are plotted as a function of delay time relative to the theoretical arrival time for an interface at 90 km depth (assuming the AK135 background velocity model). The 90 km and 0 km marks are drawn as horizontal black lines in all panels. The gray lines mark the location of significant anisotropic boundaries and are labeled with the delay time relative to the direct-P arrival. The same boundaries are also marked in the bottom panels of (B) in Figures 7-9. Rose plots that display the transverse component RF energy as a function of backazimuth for the time window associated with these boundaries are shown in Figure 15. Magenta bars correspond to approximate MLD arrival delay times (±0.5 seconds). The cyan line corresponds to the Moho arrival.

Figure 7. Ps receiver functions binned as a function of harmonic expansion terms for Superior Province stations ECSD, ULM and AGMN. Plotting conventions are as in Figure 6. The boundaries marked with gray lines on this figure are also marked in the

bottom panels of (B) in Figures 10-12. Corresponding rose plots for these boundaries are shown in Figure 15.

Figure 8. Ps receiver functions for station EGMT stacked and binned as a function of (A) epicentral distance and (B) backazimuth. (A) and (B, top panel) show radial component RFs, while (B, bottom panel) shows transverse component RFs. Blue phases correspond to a velocity increase with increasing depth, red phases correspond to a velocity decrease with depth. (A) Horizontal cyan line marks the location of the inferred Moho arrival (see Figure 5 and Table 1); magenta lines mark negative phases which may correspond to MLDs (see Figure 5 and Table 1). The predicted arrival window for the first crustal multiple is shown in semi-transparent blue at the bottom (~18 seconds at 30° epicentral distance) of the figure. (B, bottom panel) Gray horizontal lines indicate the location of anisotropic boundaries as inferred from the harmonic regression analysis shown in Figure 6. The rose diagrams for these boundaries are shown in Figure 15.

Figure 9. Ps receiver functions for station K22A binned as a function of (A) epicentral distance and and (B) back azimuth. In (A), the predicted arrival window for multiples resulting from conversions at the base of a thick (2-4 km) sedimentary sequence are shown in semi-transparent blue and red in the 2-6 seconds. All other plotting conventions are as in Figure 8.

Figure 10. Ps receiver functions for station RSSD binned as a function of (A) epicentral distance and and (B) back azimuth. Plotting conventions are as in Figure 8.

Figure 11. Ps receiver functions for station ECSD binned as a function of (A) epicentral distance and and (B) back azimuth. Plotting conventions are as in Figure 8.

Figure 12. Ps receiver functions for station AGMN binned as a function of (A) epicentral distance and and (B) back azimuth. Plotting conventions are as in Figure 8.

Figure 13. Ps receiver functions for station ULM binned as a function of (A) epicentral distance and and (B) back azimuth. Predicted crustal multiples arrivals are shown with semi-transparent blue and red lines at 12-16 seconds. Plotting conventions are as in Figure 8.

Figure 14. Radial and transverse component Ps receiver functions, binned as a function of back azimuth, and modeled and unmodeled portions of the harmonic expansion, computed for five synthetic models, each containing two layers of anisotropy. Models 1-3 have a bottom layer with a fast axis oriented at an azimuth of 60° and a dip of 55°, and a top layer dip of 0°. The azimuth of the top layer fast axis in Model 1 is 30°, 60° in Model 2, and 0° in Model 3. The fast axis orientation of the top layer in Models 4 & 5 is 0° azimuth and 0° dip, while the bottom layer fast axis azimuth/dip in Model 4 is 60°/0° and in Model 5 is 90°/0°.

Figure 15. Transverse component Ps receiver function rose plots for inferred anisotropic boundaries marked in Figures 6-12. Stations are arranged from west to east; the vertical

axis represents delay time (with respect to the direct P arrival time). Each individual rose plot shows the transverse component amplitudes as a function of backazimuth at the given delay time. For each station, the left-hand column rose plots correspond to the observed amplitudes in the RF data, as shown in Figures 7-12. The right-hand column for each station corresponds to the best fitting model for the given delay time computed from the harmonic regression (Figures 5 and 6). Individual rose plots (data and model) were normalized such that the maximum amplitude within each plot is equal to one. The gray boxes correspond to the delay time (± 0.5 seconds) of the MLD/LAB picks shown in Figure 5 and listed in Table 1.

Table 1. Table of inferred Moho and MLD delay time picks and approximate depths, calculated assuming the AK135 velocity model, as shown on the stacked radial RFs in Figure 5. The network and number of events used in the receiver function analysis are also listed.

Figure 1. Figure

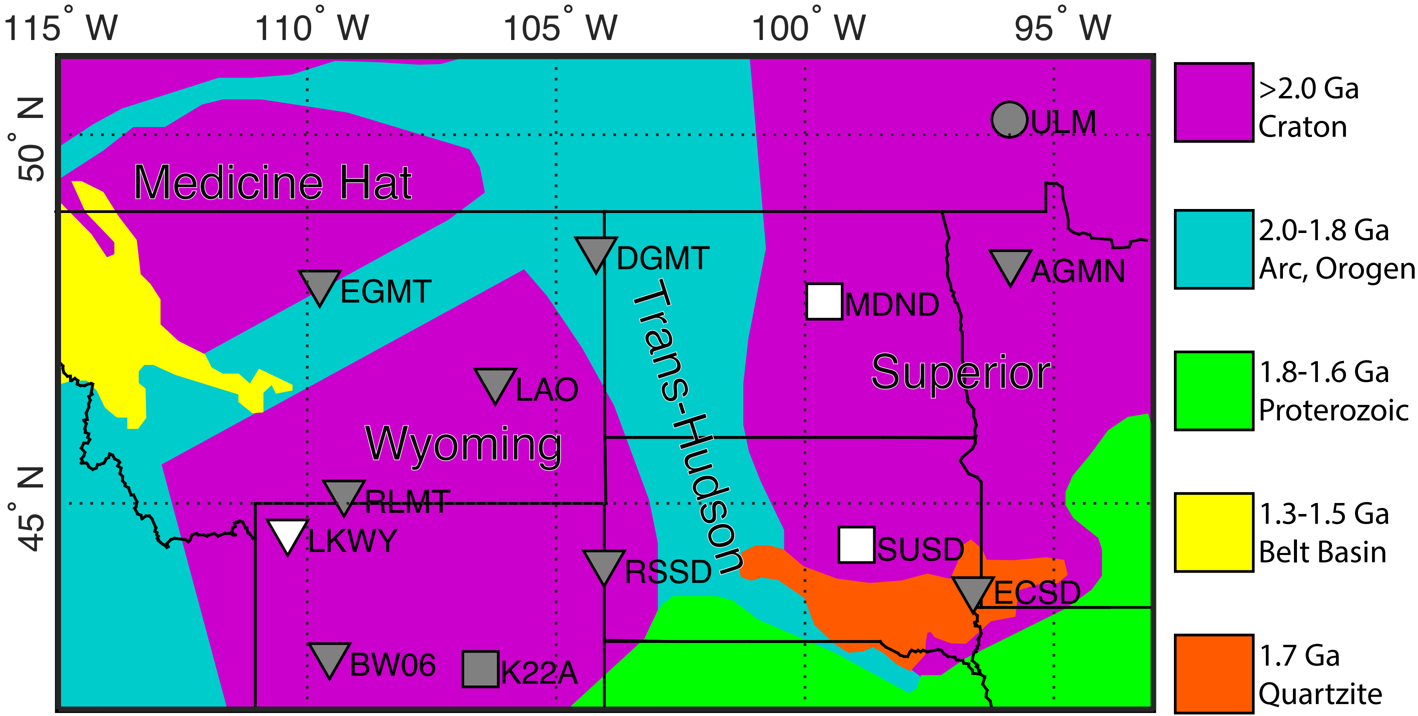

115° W
110° W
105° W
100° W
95° W
50° N
45° N
Medicine Hat
Wyoming
Trans-Hudson
Superior
ULM
DGMT
AGMN
EGMT
MDND
LAO
RLMT
LKWY
RSSD
SUSD
ECSD
BW06
K22A
>2.0 Ga Craton
2.0-1.8 Ga Arc, Orogen
1.8-1.6 Ga Proterozoic
1.3-1.5 Ga Belt Basin
1.7 Ga Quartzite

Figure 2. Figure

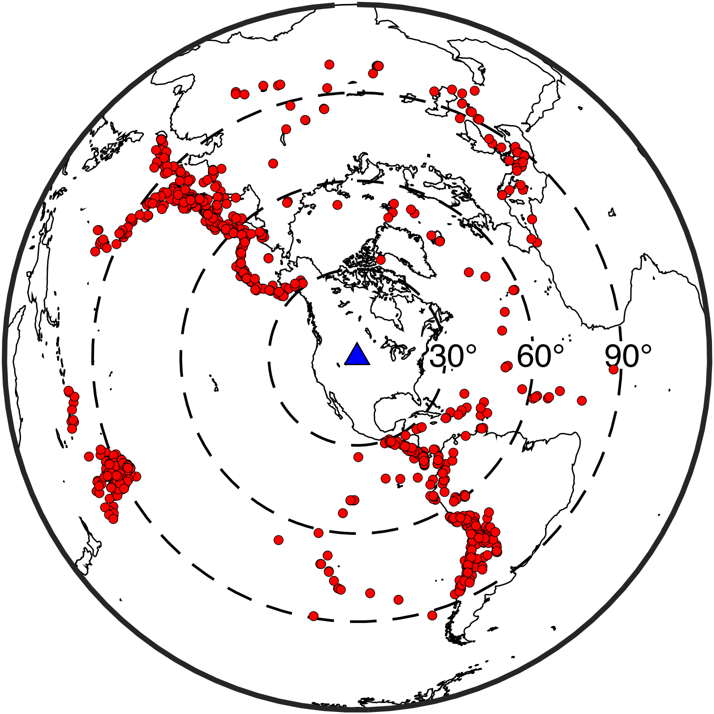
30°
60°
90°

Figure 3. Figure

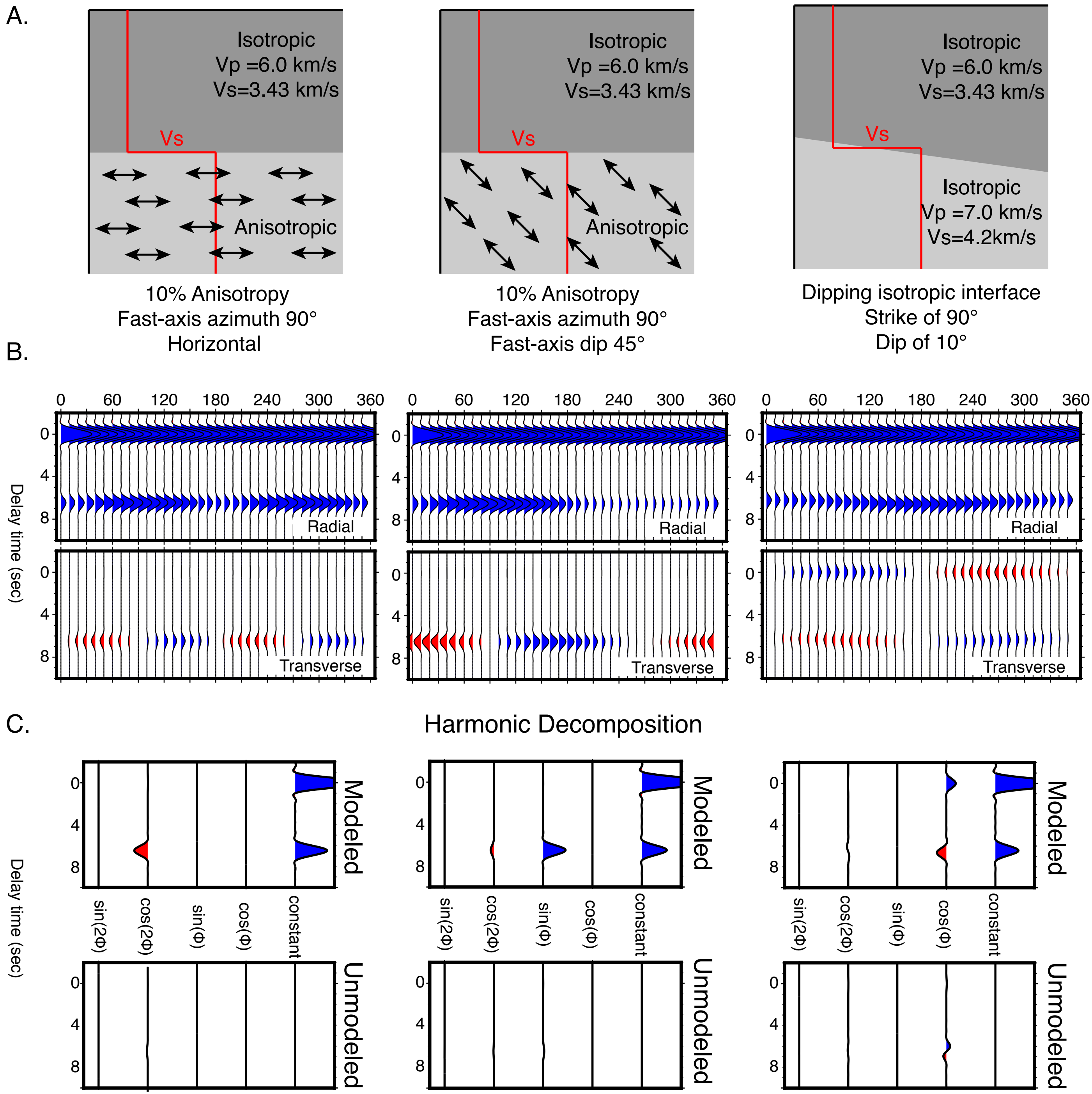
A.
Isotropic
Vp =6.0 km/s
Vs=3.43 km/s
Vs
Anisotropic
10% Anisotropy
Fast-axis azimuth 90°
Horizontal
Isotropic
Vp =6.0 km/s
Vs=3.43 km/s
Vs
Anisotropic
10% Anisotropy
Fast-axis azimuth 90°
Fast-axis dip 45°
Isotropic
Vp =6.0 km/s
Vs=3.43 km/s
Vs
Isotropic
Vp =7.0 km/s
Vs=4.2km/s
Dipping isotropic interface
Strike of 90°
Dip of 10°
B.
0 60 120 180 240 300 360
Delay time (sec)
Radial
Transverse
C.
Harmonic Decomposition
Delay time (sec)
Modeled
Unmodeled
sin(2Φ)
cos(2Φ)
sin(Φ)
cos(Φ)
constant

Figure 4. Figure

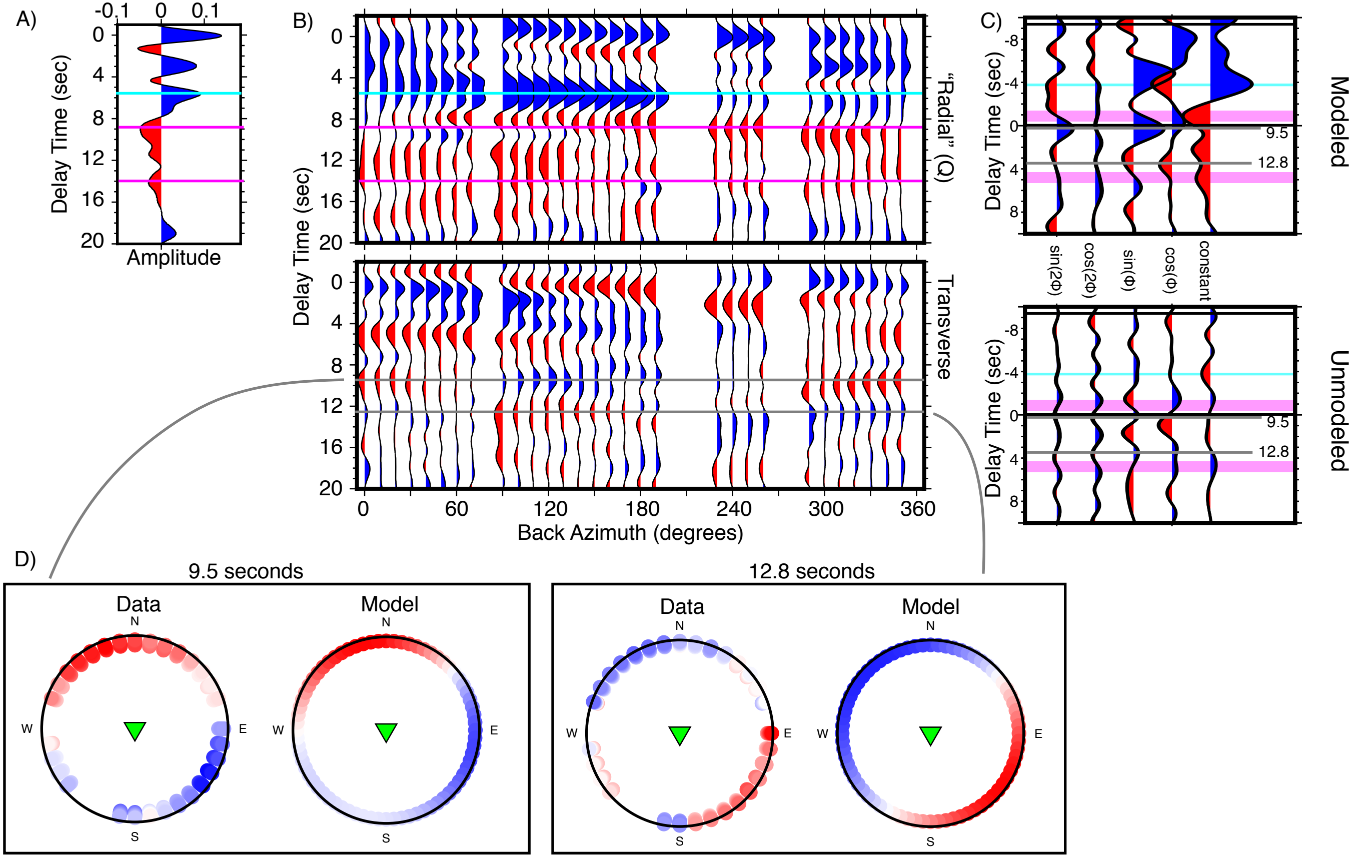

A)
B)
C)
D)
Delay Time (sec)
Amplitude
"Radial" (Q)
Transverse
Back Azimuth (degrees)
Modeled
Unmodeled
sin(2Φ)
cos(2Φ)
sin(Φ)
cos(Φ)
constant
9.5
12.8
9.5 seconds
12.8 seconds
Data
Model
N
E
S
W

Figure 5. Figure

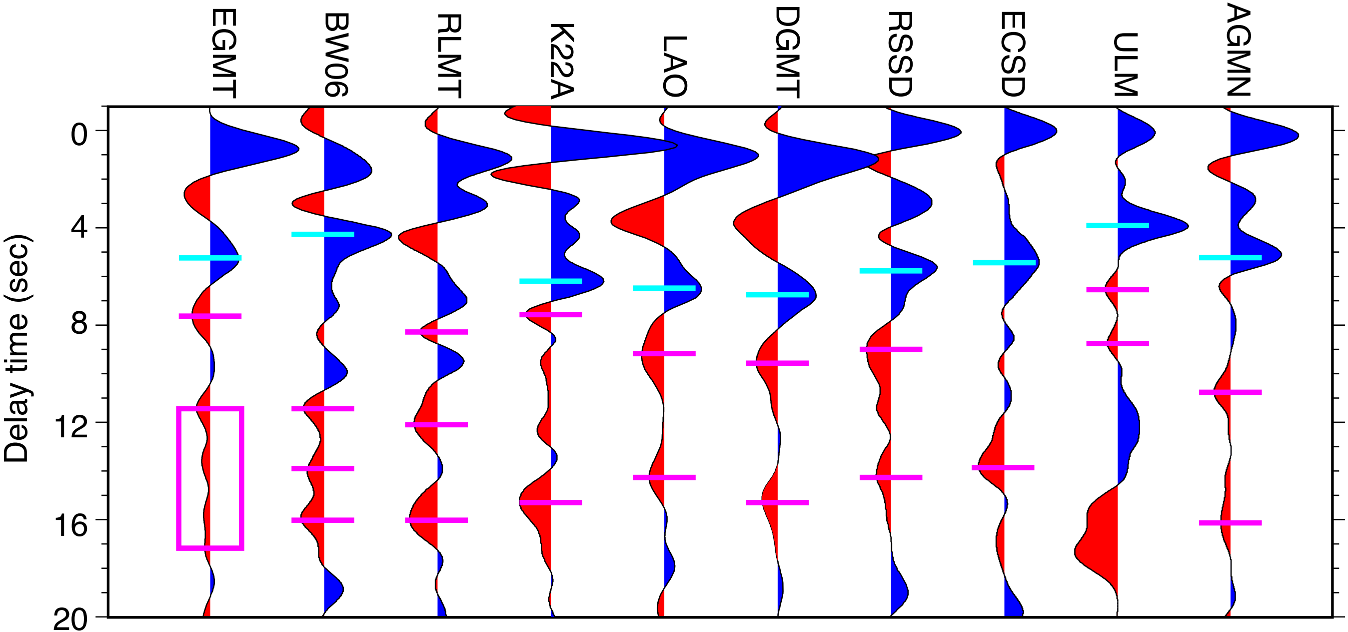
EGMT
BW06
RLMT
K22A
LAO
DGMT
RSSD
ECSD
ULM
AGMN
Delay time (sec)
0
4
8
12
16
20

Figure 6. Figure

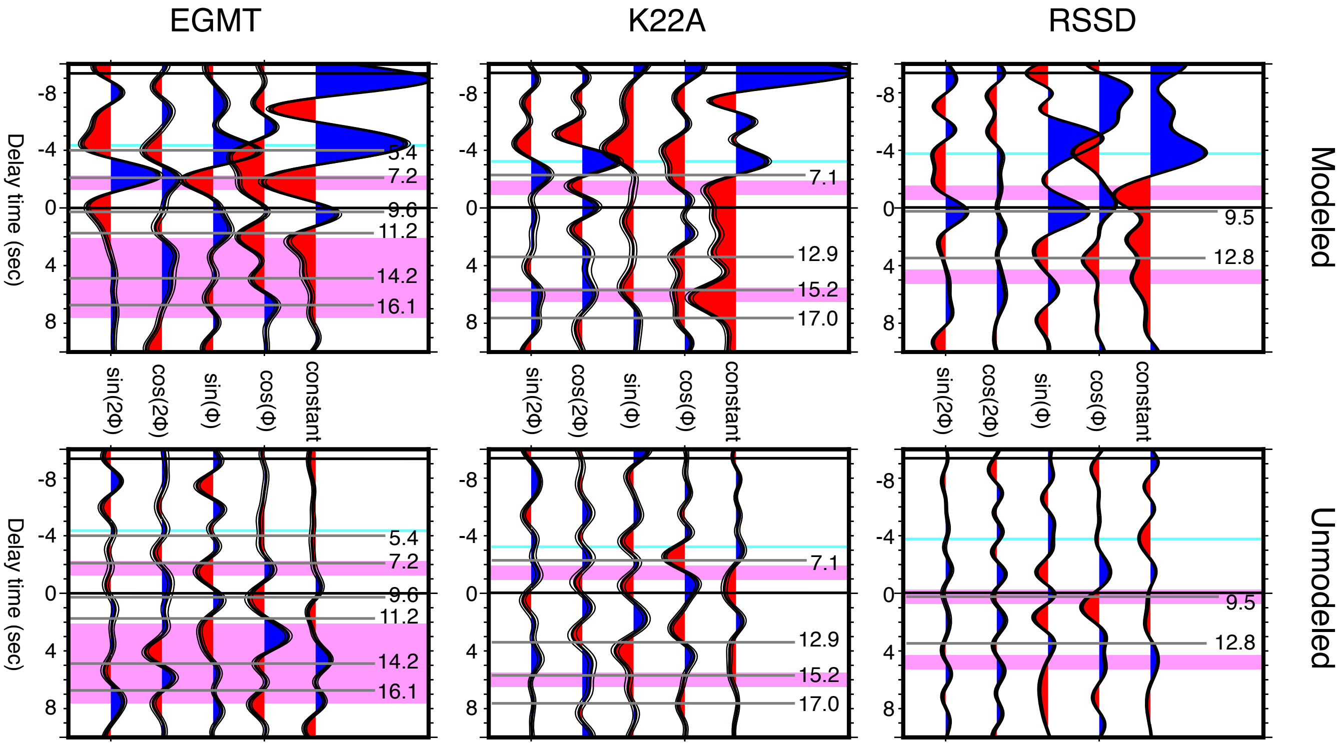
EGMT
K22A
RSSD
Modeled
Unmodeled
Delay time (sec)
-8
-4
0
4
8
sin(2Φ)
cos(2Φ)
sin(Φ)
cos(Φ)
constant
5.4
7.2
9.6
11.2
14.2
16.1
7.1
12.9
15.2
17.0
9.5
12.8

Figure 7. Figure

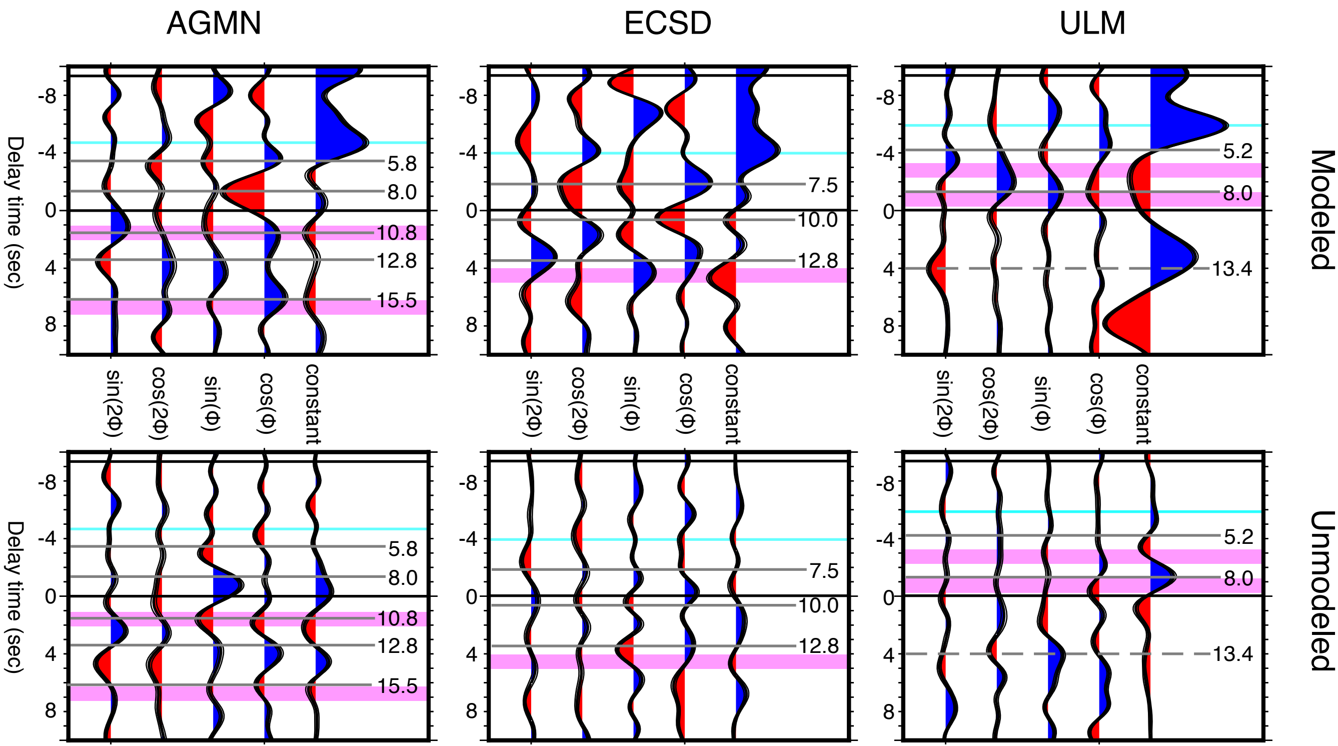

AGMN
ECSD
ULM
Modeled
Unmodeled
Delay time (sec)
-8
-4
0
4
8
5.8
8.0
10.8
12.8
15.5
7.5
10.0
12.8
5.2
8.0
13.4
sin(2Φ)
cos(2Φ)
sin(Φ)
cos(Φ)
constant

Figure 8. Figure

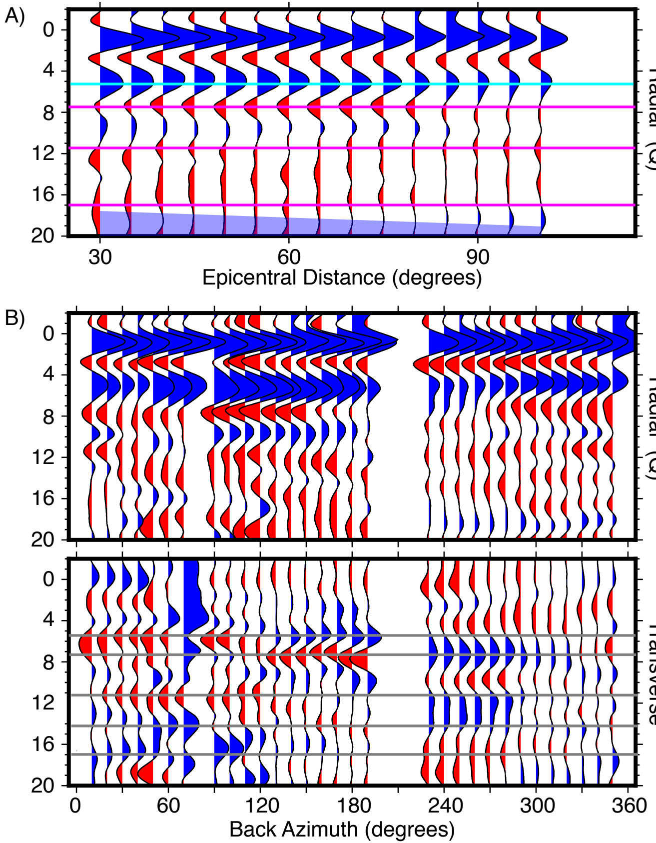

A)
0
4
8
12
16
20
30
60
90
Epicentral Distance (degrees)
"Radial" (Q)
B)
0
4
8
12
16
20
"Radial" (Q)
Transverse
0
60
120
180
240
300
360
Back Azimuth (degrees)

Figure 9. Figure

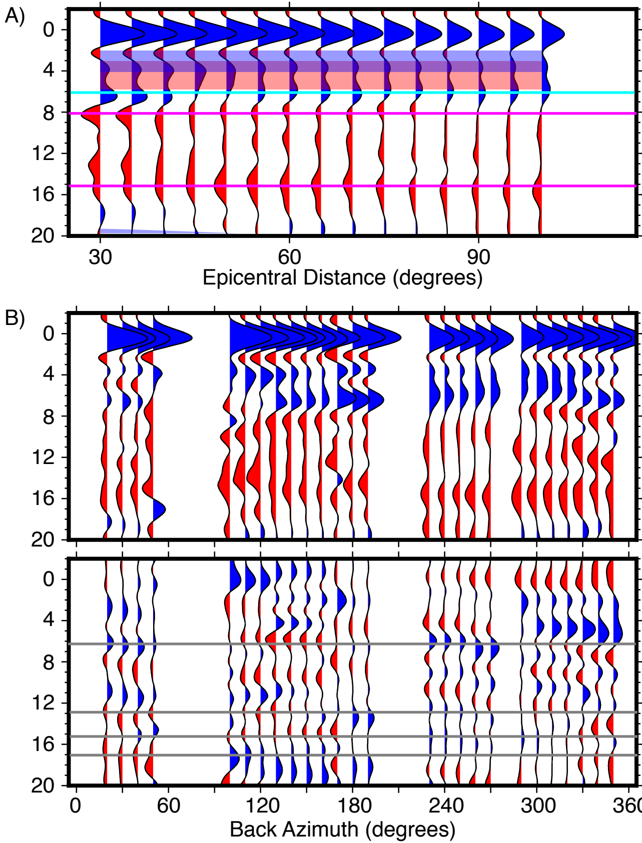

A)
0
4
8
12
16
20
30
60
90
Epicentral Distance (degrees)
"Radial" (Q)
B)
0
4
8
12
16
20
"Radial" (Q)
0
4
8
12
16
20
Transverse
0
60
120
180
240
300
360
Back Azimuth (degrees)

Figure 10. Figure

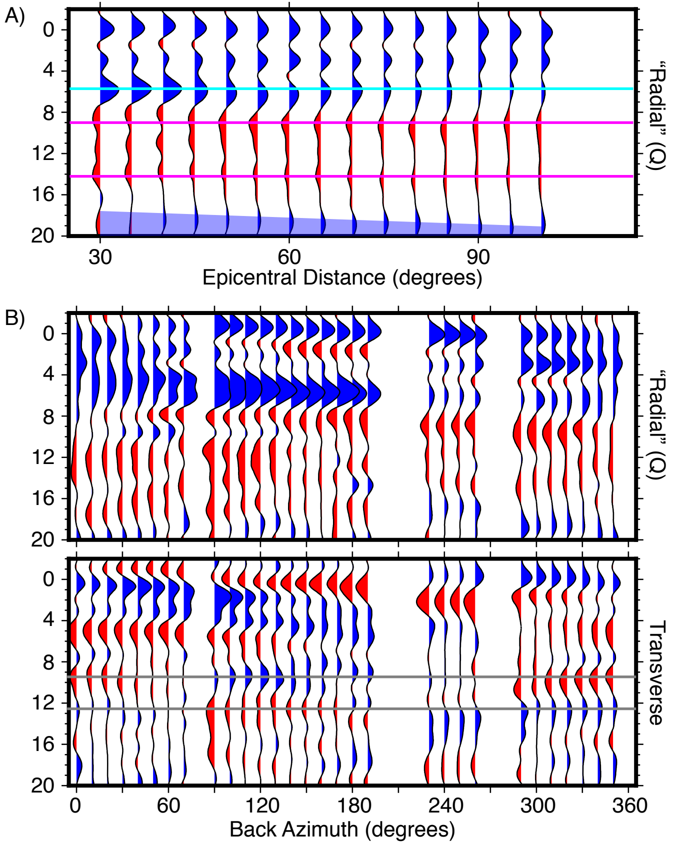

A)
"Radial" (Q)
Epicentral Distance (degrees)
30
60
90
0
4
8
12
16
20
B)
"Radial" (Q)
Transverse
Back Azimuth (degrees)
0
60
120
180
240
300
360

Figure 11. Figure

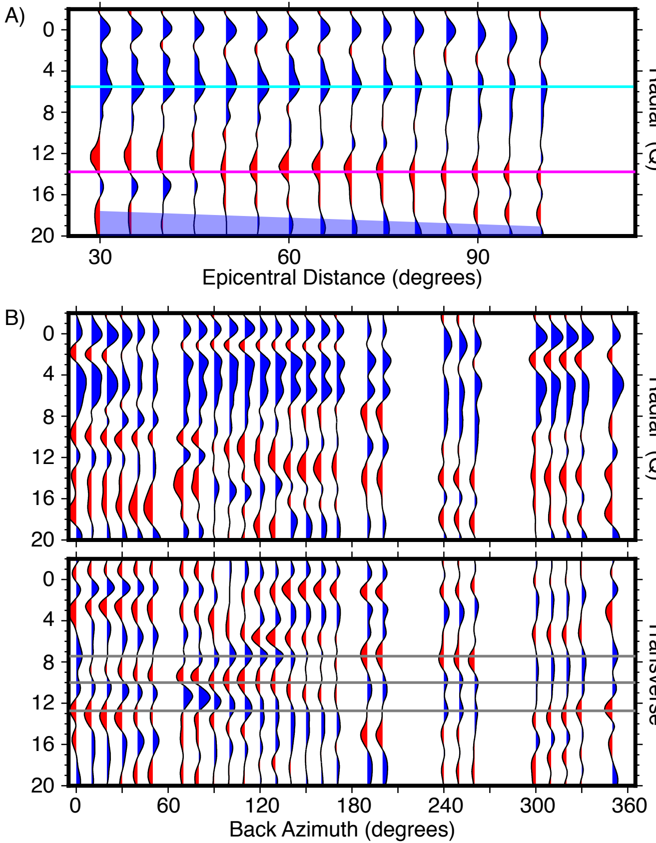

A)
0
4
8
12
16
20
30
60
90
Epicentral Distance (degrees)
"Radial" (Q)
B)
0
4
8
12
16
20
"Radial" (Q)
0
4
8
12
16
20
Transverse
0
60
120
180
240
300
360
Back Azimuth (degrees)

Figure 12. Figure

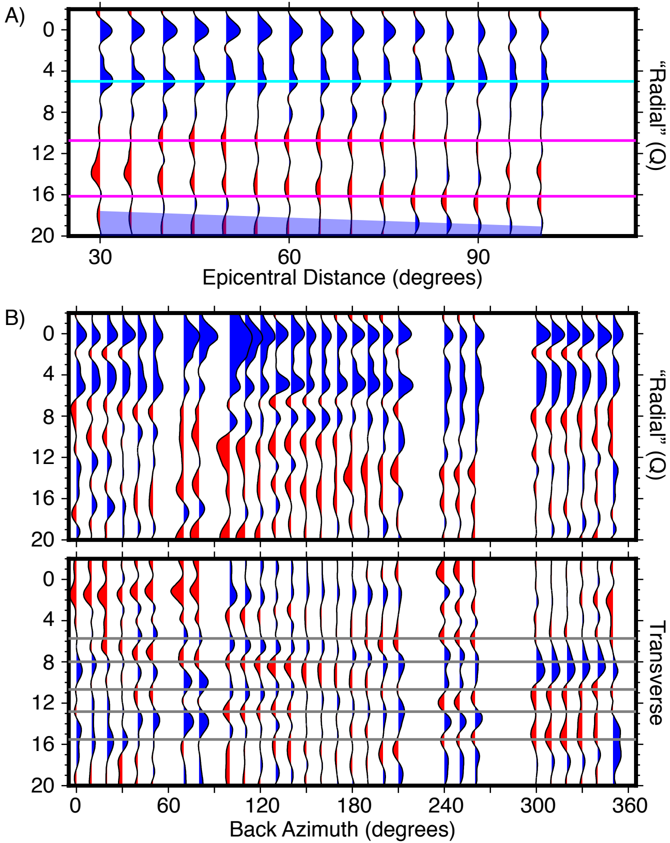

A)
0
4
8
12
16
20
30
60
90
Epicentral Distance (degrees)
"Radial" (Q)
B)
0
4
8
12
16
20
"Radial" (Q)
0
4
8
12
16
20
Transverse
0
60
120
180
240
300
360
Back Azimuth (degrees)

Figure 13. Figure

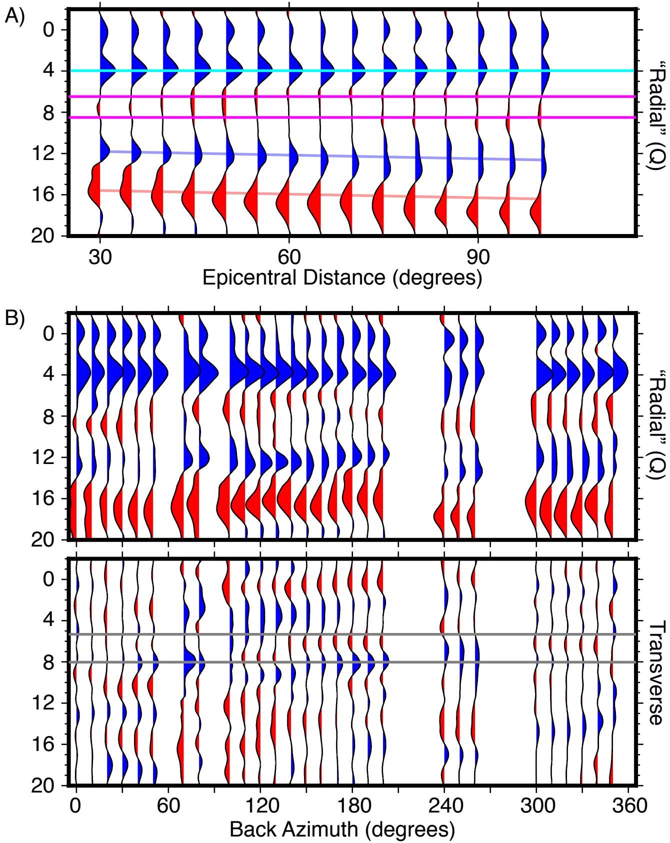

A)
0
4
8
12
16
20
"Radial" (Q)
30
60
90
Epicentral Distance (degrees)
B)
0
4
8
12
16
20
"Radial" (Q)
0
4
8
12
16
20
Transverse
0
60
120
180
240
300
360
Back Azimuth (degrees)

Figure 14. Figure

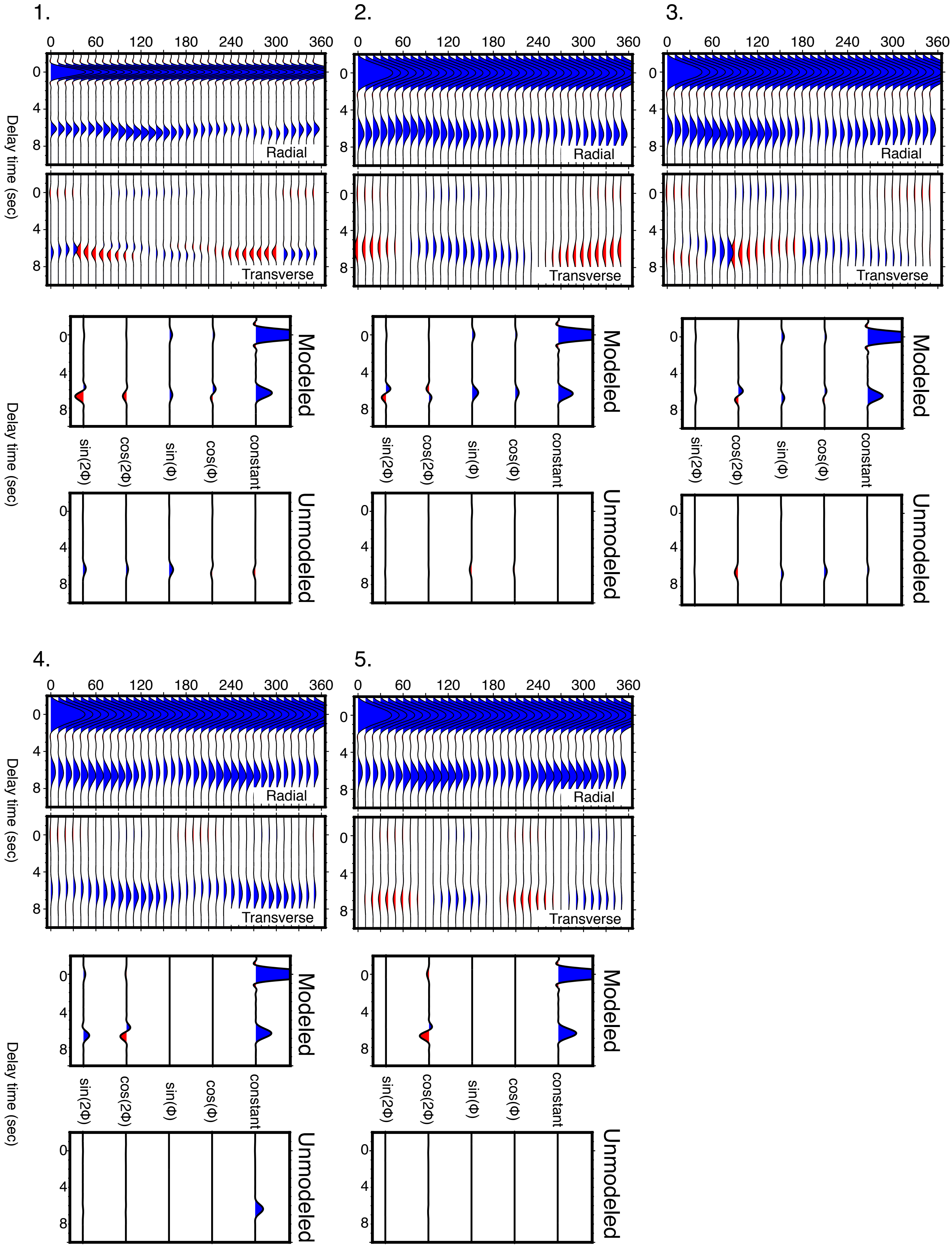
1.
2.
3.
4.
5.
0 60 120 180 240 300 360
Delay time (sec)
0 4 8
Radial
Transverse
Modeled
Unmodeled
sin(2Φ)
cos(2Φ)
sin(Φ)
cos(Φ)
constant

Figure 15. Figure

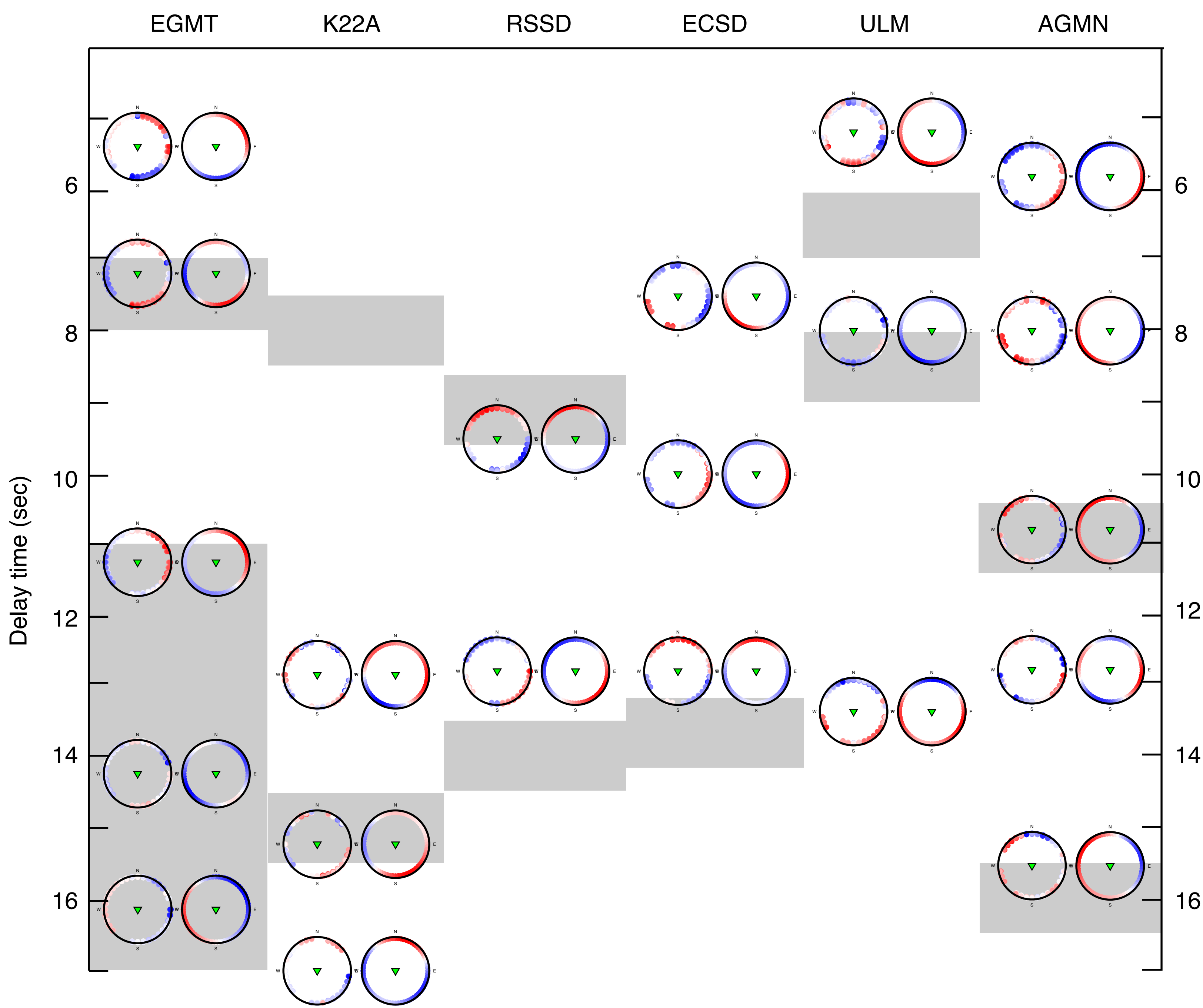

EGMT
K22A
RSSD
ECSD
ULM
AGMN
Delay time (sec)
6
8
10
12
14
16
N
S
W
E

			Moho		Negative/MLD					
Network	Name	# of Events	time[1] (sec)	depth[2] (km)	time[1] (sec)	depth[2] (km)	time[1] (sec)	depth[2] (km)	time[1] (sec)	depth[2] (km)
US	**AGMN**	464	**5.2**	47	**10.8**	105	**16.1**	158		
US	**BW06**	967	**4.3**	39	**11.3**	110	**14**	137	**16**	157
US	**DGMT**	604	**6.8**	59	**9.5**	92	**15.2**	149		
US	**ECSD**	449	**5.4**	50	**13.8**	135				
US	**EGMT**	731	**5.3**	49	**7.6**	72	**11.4-17.1**	111-168		
TA	**K22A**	588	**6.2**	58	**8**	76	**15.3**	150		
US	**LAO**	717	**6.5**	61	**9.3**	90	**14.2**	139		
US	**RLMT**	585	**NA**	NA	**8.2**	78	**12**	117	**16**	157
US	**RSSD**	898	**5.7**	53	**9**	86	**14.2**	139		
CN	**ULM**	573	**3.9**	35	**6.5**	61	**8.6**	82		
US	**LKWY**	823								
TA	**MDND**	421								
TA	**SUSD**	331								

Note 1: Time corresponds to delay time relative to the direct-P arrival
Note 2: Depth is estimated for a vertically incident wave, assuming AK135